Firebrands Generated During WUI Fires: A Novel Framework for 3D Morphology Characterization

Nicolas Bouvet (iD)*, *National Institute of Standards and Technology (NIST), Gaithersburg, USA*
Minhyeng Kim (iD), *Fire & Risk Alliance, LLC, Rockville, USA*

Abstract. The goal of the present work is to establish a framework for firebrand morphology characterization. Central to this framework is the development of a simple firebrand shape classification model using multi-dimensional particle shape descriptors. This classification model is built upon a series of synthetically generated 3D particles whose shapes and sizes are chosen to be representative of actual firebrands typically encountered during vegetative and structural fuel burns. Principal Component Analysis (PCA) is applied to the synthetic dataset and used to structure the classification model. The model is then verified using 3D digital representations of real-world particles (firebrands collected during tree burns and unburned bark pieces from oak trees). The classification model, which will allow meaningful comparisons of firebrand morphological features by shape class, is expected to be gradually refined as more datasets are made available throughout the Wildland–Urban Interface (WUI) fire research community.

1. Introduction

The significance of firebrand activity during wildland and wildland–urban interface (WUI) fires has been highlighted by many post-fire investigations [1–5] in which it is often found that structure losses are, for a large part, triggered by firebrands (either involving direct or indirect ignition events) rather than direct contact with the main fire front. Hence, better understanding the characteristics of the large amounts of firebrands produced during these fires, often in the form of "showers" or "rains" of burning particles, has become a point of paramount importance. Central to the firebrand shower problem is firebrand morphology. From airborne particle generation to recipient fuel ignition, firebrand shape is a key parameter in many analytical and experimental studies. It often constitutes a

---

* Correspondence should be addressed to: Nicolas Bouvet, E-mail: nicolas.bouvet@nist.gov

fundamental assumption around which generation and transport models are built. For instance, Barr and Ezekoye [6] modeled firebrand breakage from tree branches using a fractal approach with cylindrical fibers as base geometry. This geometry strongly influences the formulation of the thermo-mechanical model proposed by the authors. Studies devoted to firebrand transport (lofting, propagation) also heavily rely on firebrand shape assumptions (see for instance Refs [7, 8]) which are essential to model proper airborne particle dynamics, via the computation of appropriate lift/drag forces. Most recent developments in firebrand transport also include modeling of the particle rotational motions [9–11], which involves computation of the particle moments of inertia, and hence requires a detailed understanding of the firebrand 3D shapes. The significance of firebrand shape has also been demonstrated in experimental works. Laboratory studies have found that firebrand thermal outputs largely depend on firebrand geometries, and that for a given shape, firebrand orientation with respect to the incident wind may be an influencing parameter [12, 13]. Ganteaume et al. [14] found that fuel bed ignition is strongly correlated with firebrand type (twigs, bark plates, bark and leaves), which encapsulates the effect of both firebrand shape and firebrand physicochemical properties. Yet to be studied, firebrand ground crawling motions (commonly observed during WUI fire events), subsequent formation of piles, and pile stability, are likely to be strongly influenced by particle morphology, as it is the case in many debris flow problems, see for instance [15–17].

To date, the morphology of firebrands generated during vegetative and structural fires has been documented almost exclusively via the measurement of particle projected areas, also referred to as cross-sections or cross-sectional areas. Typically, firebrands produced during fire experiments are water-quenched at ground level, dried, and arranged on a flat surface in their most mechanically stable position. A top-view photograph is usually taken, and firebrand projected areas are then extracted via computerized procedures provided that spatial resolution is known [18–30]. Alternatively (or simultaneously), some firebrand characteristic dimensions, e.g., diameter or thickness, are obtained via caliper measurements [21, 22, 31–33]. A second approach consists in measuring, using similar imaging techniques, the areas of holes left by the firebrands in substrates adequately chosen [34–37], and consider these measurements as true representations of the firebrand projected areas. The last approach, most recent, is geared towards airborne firebrands: 2D imaging devices (IR and/or visible cameras) are used to record in flight firebrands and their projected areas (with respect to the device image plane) are extracted at all relevant timesteps [20, 38–43]. As firebrands may tumble, these areas may considerably vary over time, hence some sort of filtering is usually applied to the time series (maximum, average, etc.). Because the 2D treatment of the firebrand sizing information is largely facilitated by well-established image processing tools, the approaches described above have been rather popular. It is important to acknowledge, however, that addressing firebrand morphology solely based on a projected area standpoint is insufficient to tackle many of the problems highlighted in the previous paragraph. Hence a framework for firebrand 3D morphology characterization is highly desirable. Such a framework is expected to: (1) promote data acquisition of firebrand 3D morphological features in a complete

and archival manner: to ensure usefulness of the data for a large variety of problems, datasets should allow queries on any morphological attributes of the firebrands, independently of the original scope of the study; (2) facilitate firebrand shape and size comparison across experimental cases: the framework should provide a base methodology for meaningful dataset comparison, thus avoiding arbitrary or subjective choices to be made (e.g., criteria/threshold to be used to classify and compare firebrand data in term of shape, characteristic length, etc.). This should allow performing targeted statistical analyses within clearly defined firebrand shape categories (see Ref. [44] for an example of such an analysis on cylindrical firebrands) in order to provide valuable inputs towards the computational modeling of firebrand flows.

The characterization of solid, non-reacting particle morphology is not a new problem: the works of Zingg [45], Krumbein [46] or Sneed and Folk [47] come to mind as early seminal contributions in the domain of pebble shape characterization. Because particle morphology, and more precisely particle shape, is essential to understand a broad range of phenomena including particle transport, deposition/sedimentation, packing, flowability, etc., particle shape characterization has been central to many scientific investigations in the fields of geology, sedimentology, and powder technology. Typically, some morphological attributes of the particles of interest are directly measured (either manually and/or via image analysis) and some indices, often referred to as descriptors, are calculated to quantify some attributes of the particle shapes (e.g., elongation, flatness, circularity). The reader is referred to the reviews by Pons et al. [48] and Blott and Pye [49] for an overview of the descriptors conventionally used (mostly 1D and 2D), as well as examples of shape classification diagrams that may result [49]. Recent works have leveraged advances in 3D visualization diagnostics (3D scanning [50–57] and X-ray computed tomography [52, 58–65]) to fully digitize particles in 3D, allowing more reliable shape characterization using complex 3D particle shape descriptors. This has led to powerful methodologies to classify particles with complex shapes and to compare particle population morphologies, see for instance the work of Parra-Denis et al. on intermetallic particles of aluminum alloys [58, 66]. It is believed that the firebrand morphology problem can greatly benefit from these approaches. The advent of low cost/high performance handheld 3D scanning devices renders the task of digitizing ground-collected firebrands not only feasible, but also time and cost-effective. Additionally, it has been shown that 3D models of airborne firebrands may also be generated via 3D imaging techniques [67], allowing shape analysis to be performed without physical collection of particle samples.

The goal of the present work is to propose a framework for firebrand morphology characterization. Central to this framework is the development of a simple firebrand shape classification model using multi-dimensional particle shape descriptors. The model is built upon series of synthetically generated 3D particles whose shapes and sizes are consistent with literature reports. Principal Component Analysis (PCA) is applied to the synthetic dataset and used to structure the classification model. The model is then verified using 3D digital representations of real-world particles (firebrands and unburned bark pieces from trees).

2. Development of the Firebrand Shape Classification Model

2.1. Expected 3D Firebrand Sizes and Shapes: A Literature Survey

As alluded to before, studies that have reported on firebrand morphology are almost exclusively focused on the determination of firebrand projected areas, also referred to as cross-sectional areas. Actual shapes of firebrands are rarely addressed, nor used as a mean of categorization in quantitative approaches (to the exception of Refs [31, 68]), although a few studies have provided pictures of collected firebrand samples, which offers a valuable glimpse at typical shape classes that may be expected. To ensure that the classification model is built upon realistic firebrand size and shape information, relevant firebrand investigations have been compiled in Table 1 for vegetative fuels and Table 2 for structural fuels. Most studies listed have provided some sort of mapping of the firebrand projected areas, which allows for an evaluation of their upper bounds. If available, other useful quantitative information regarding the firebrand morphology has been added in the *Notes* column. While the listings provided in Table 1 and 2 intend to be as broad as possible, the rather limited number of studies available and uniqueness of each approach (in terms of experimental conditions, firebrand collection and data processing methodologies, etc.) do not yield universal conclusions regarding firebrand generation, but still offer a reasonable basis to guide synthetic particle generation.

The following observations can be made considering both Table 1 and 2; for vegetative fuels, it can be assumed that almost all available firebrand projected area datasets fall below the 10 cm^2 mark, with most of the data being contained below the 5 cm^2 threshold. Aside from Ref. [36], very large firebrands, considered as outliers, tend to fall within the 10 cm^2 to 30 cm^2 range (e.g., burning leaves in Ref. [39]). Measured projected areas for structural fuels display higher variability, with almost all datasets contained below 25 cm^2, and most data located below the 10 cm^2 mark. Few very large outliers have been recorded in the 25 cm^2 to 130 cm^2 range (likely due to dimensionally large components such as wood studs [27, 28], OSB [28] or roofing paper [29]), these outliers tend to be significantly larger than their vegetative counterparts. Note that the firebrand projected area limits as reported in Table 1 and 2 are voluntarily conservative to ensure the widest possible span of parameters for synthetic particle generation. These limits do not necessarily correspond to a fixed percentage of the total number of firebrands collected during each test.

Upon close examination of the sample images provided by some of the studies listed in Table 1 and 2 (see last column), it can be asserted that firebrand shapes may be classified into several categories. To facilitate the discussion that follows, we adopt the minimum bounding box (MBB) convention proposed by Blott and Pye [49] and consider that the three main dimensions of a particle, referred to as *long* (L), *intermediate* (I) and *small* (S), equates the corresponding side lengths of the smallest imaginary box which can contain the particle. Hence, the firebrand shape categories are identified as follows: (1) *Rods*, which gather thin and elongated particles (small S and I, large L). Mostly firebrands made of branches, twigs

Table 1
Firebrand Morphology/Vegetative Fuels

First author/year/reference	Test case	Firebrand projected areas	Notes	Firebrand picture?
Zen 2021 [38]	Prescribed fires/NJ Pine Barrens	All < 4 cm^2 (most < 1 cm^2)	Airborne (PA def.: maximum projected area)	Yes
Almeida 2021 [39]	Lab. study (no wind)/small trees: cork oak, English oak, blue gum, pine	Almost all < 10 cm^2 (most < 5 cm^2)	Airborne (PA def.: average projected area); some large brands (leaves) with PA < 16 cm^2	No
Hudson 2020 [18]	Single tree, outdoor/Douglas-fir, grand fir, western juniper, ponderosa pine	All < 1.10 cm^2 (most < 0.5 cm^2)	GC (water trays); some work also performed with fire-resistant fabric	No
Filkov 2018 [40]	Prescribed fires/NJ Pine Barrens	Almost all < 5 cm^2	Airborne (PA def.: unknown); small firebrand detection issues reported as compared to ground collection measurements	No
Thomas 2017 [19]	Prescribed fire/NJ Pine Barrens	Almost all < 5 cm^2 (most < 2 cm^2)	GC (water cans)	Yes
Filkov 2017 [20]	Prescribed fires/NJ Pine Barrens	Almost all < 5 cm^2 (most < 2 cm^2)	GC (water pans—w & w/ plastic film); Airborne (PA def.: unknown); IR footage: most brands with PA < 1 cm^2, largest brand PA ~ 7 cm^2	Yes
El Houssami 2016 [31]	Prescribed fire/NJ Pine Barrens	Almost all < 5 cm^2 (most < 2 cm^2)	GC (water pans—w & w/plastic film); barks/branches in the 1 mm to 6 mm thickness range	Yes
Kapcak 2015 [68]	Prescribed fires/Canadian boreal forest, NT	NA	GC (water pans—some with a vertical screen), tarp, sheet with fire retardant; burn marks on sheets: majority < 0.10 cm^2	Yes
Manzello 2014 [37]	2007 Angora fire	Almost all < 4 cm^2 (most < 0.5 cm^2) Some > 10 cm^2	Trampoline data; largest hole ~ 10.25 cm^2	No
Almeida 2014 [41]	Lab. study (no wind)/barks and shrubs from Eucalyptus tree		Airborne (PA def.: unknown); largest firebrand PA ~ 29 cm^2	No
Rissel 2013 [36]	2011 Bastrop complex fire	Almost all < 3 cm^2 (most < 0.5 cm^2)	Trampoline data; largest hole ~ 176 cm^2	No

Table 1
continued

First author/year/reference	Test case	Firebrand projected areas	Notes	Firebrand picture?
Manzello 2009 [32]	Single tree, indoor (no wind) Korean pine	Almost all < 10 cm^2 (most < 5 cm^2) largest PA ~ 15 cm^2 (estimated from provided firebrand surface areas)	GC (water pans); firebrand surface area: all < 50 cm^2 (most < 15 cm^2); firebrand max. length: < 300 mm/max. diameter < 15 mm	Yes
Gould 2008 [69]	Prescribed fires/Southern Australia eucalypt forests	NA	GC (plastic sheets); large proportion of firebrands: small flakes (bark) typically 2 to 4 mm thick	No
Manzello 2007 [33]	Single tree, indoor (no wind) Douglas fir	Almost all < 8 cm^2 (most < 3 cm^2) largest PA ~ 12 cm^2 (estimated from provided firebrand surface areas)	GC (water pans); firebrand surface area: all < 40 cm^2 (most < 10 cm^2); firebrand max. length: < 200 mm/max. diameter < 12 mm	Yes

GC ground collection, *PA* projected area, *def.* definition

Table 2
Firebrand Morphology/Structural Fuels

First author/year/reference	Test case	Firebrand projected areas	Notes	Firebrand picture?
Suzuki 2021 [21]	Cedar shingle/shakes roofing (with wind)	Almost all < 25 cm² (most < 10 cm²)	GC (water pans); firebrand max. thicknesses up to 2 cm, down to below 0.1 cm; largest firebrand with PA ~ 130 cm²	No
Suzuki 2020 [22]	Plywood roofing (with wind)	All < 20 cm² (most < 5 cm²)	GC (water trays); firebrand max. thicknesses up to 1.3 cm	Yes
Hedayati 2019 [23]	90° Corner assemblies (with wind)	Mean < 5 cm²	GC (water pans)—(add. cases in [71])	Yes
Manzello 2019 [24]	OSB roofing assemblies (with wind)	Most < 10 cm²	GC (water pans); largest firebrand with PA ~ 40 cm²	Yes
Suzuki 2018 [25]	Urban fire	Almost all < 13 cm² (most < 5 cm²)	Post-fire collection, various sites; largest firebrand with PA ~ 130 cm²	Yes
Suzuki 2016 [26]	Wall assemblies with cedar siding (with wind)	Almost all < 25 cm² (most < 10 cm²)	GC (water pans); largest firebrand with PA ~ 110 cm² (wood stud)	Yes
Suzuki 2014 [27]	Full scale structure (with wind)	Almost all < 20 cm² (most < 10 cm²)	GC (water pans); largest firebrand ~ 45 cm²	No
Suzuki 2013 [28]	Wall/re-entrant corner assemblies (with wind)	Almost all < 25 cm² (most < 10 cm²)	GC (water pans); few large firebrands with PA > 100 cm² (wood studs, OSB)	No
Suzuki 2012 [29]	Full scale structure (outdoor)	Almost all < 10 cm²	GC (water pans); largest firebrand with PA ~ 80 cm² (roofing paper)	Yes
Yoshioka 2004 [30]	Full scale structure (with wind)	Almost all < 4 cm² (most < 2 cm²)	GC (trays with and without water)	Yes
Waterman 1969 [70]	Roof assemblies	Some firebrands > 58 cm²	Roof-level collection in water pool; firebrands sieved using 2.5 cm hexagonal mesh, 1.1 cm square mesh, and 0.3 cm mesh	Yes
Vodvarka 1969 [35]	Full scale structures (outdoor)	Almost all < 14.5 cm² (most < 3.6 cm²)	GC (plastic sheets)	No
Vodvarka 1969 [34]	Full scale structures (outdoor)	Almost all < 14.5 cm² (most < 3.6 cm²)	GC (plastic sheets); largest firebrand PA ~ 97 cm²	No

GC ground collection, *PA* projected area

and needles collected during vegetative fuel burns (see examples in Refs [19, 20, 31–33, 38, 68]) are expected to populate this class; (2) *Flats*, particles with the dimension S significantly smaller than both I and L. Available sample images suggest that this firebrand morphology is predominant for structural fuel burns [22–26, 29, 70]. For vegetative fuels, bark pieces (see examples in Refs [19, 20, 31, 38]), and likely leaves if present, will also fall in this category; (3) *Equants*, particles whose three dimensions S, I and L are roughly equivalent. Firebrand sample images hint that they are present for both vegetative and structural fuel burns (mostly in the form of small woody particles). It is interesting to note that the simple classification highlighted above echoes that originally proposed by Zingg [45] for pebbles (and later re-assessed by others, see Refs [46, 49, 56, 59, 62]). We follow Zingg's approach and subdivide the *Flats* class identified above into two distinct classes: *Blades* (small S, large L and I, with L significantly larger than I) and *Plates* (small S, large L and I, with $L \approx I$). In the case of firebrands, such subdivision is justified as plated particles offer greater surface for contact as compared to bladed particles with identical S and L dimensions, and thus, may represent an enhanced ignition risk for a recipient fuel. Large plated firebrands have been previously documented in the context of roofing component combustion (e.g., shingles and sheathing, see images in Refs [70, 72]). Lastly, it is important to recognize that some firebrands shown in the literature, that belong to the shape classes listed above, may be highly curved: this is the case for twigs and needles, e.g. [31, 33, 38], and very likely, barks [31]. As previously discussed by Vecchio et al. [59], non-convex particles may not be properly classified solely using bounding box sizing tools, as the S, I and L dimensions may not correspond to real features of the particles. Hence the use of more refined particle shape descriptors is required to achieve proper firebrand classification. This is further discussed in Sect. 2.3.

2.2. Sample Particles[1]

To ensure the widest range of applicability, the firebrand shape classification model needs to be built upon the largest possible number of firebrand shape datasets. Unfortunately, as outlined above, only a limited number of investigations is available, and none provide 3D information necessary to implement advanced classification methods. Generating the missing data by performing field experiments is de facto excluded given the tremendous number of tests required, making such an approach both cost and time prohibitive. Thus, a different approach was sought. First, synthetic particles were generated based on firebrand characteristic shapes, projected area ranges and, when available, characteristic dimensions as identified in the previous section. The classification model, built upon the synthetic particle datasets, could then be applied to 3D models of real firebrands

---

[1] Certain commercial equipment, instruments, or materials are identified in this paper in order to specify the experimental procedure adequately. Such identification is not intended to imply recommendation or endorsement by the National Institute of Standards and Technology, nor is it intended to imply that the materials or equipment identified are necessarily the best available for the purpose.
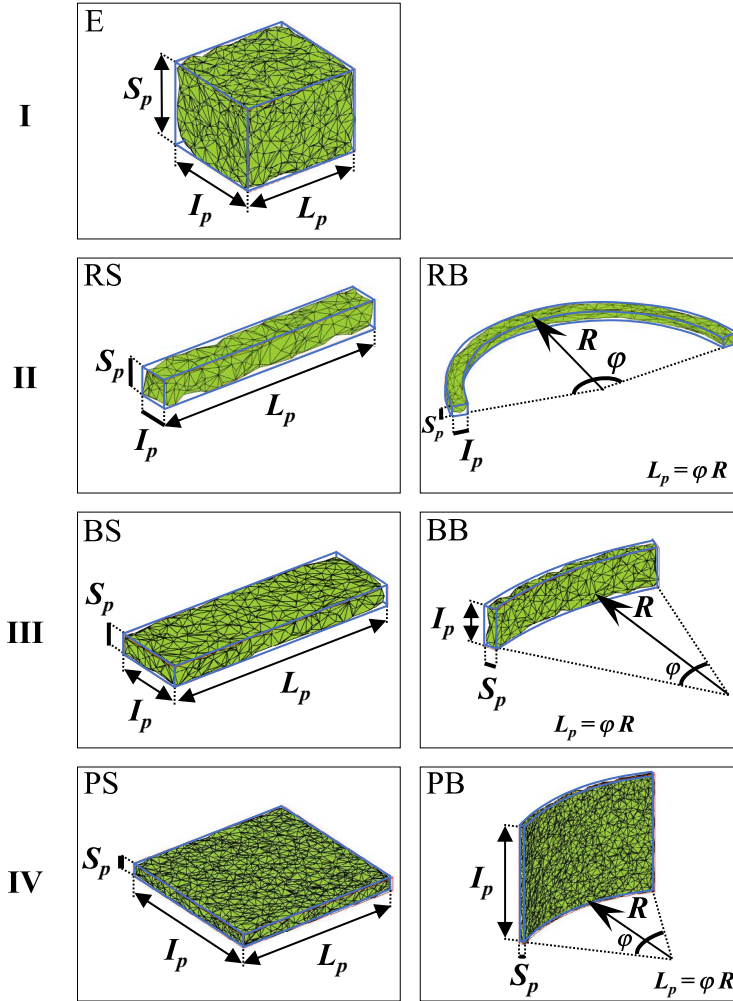
Class

Figure 1. **Example of synthetic firebrand representative of each shape class considered in this work. The virtual boxes used for particle generation are shown in blue with associated labels (L_p, I_p and S_p: box dimensions, R: radius of curvature and φ: degree of curvature). The box dimensions/curvature parameters are randomly varied as part of the particle generation process (Color figure online).**

acquired via 3D scanning. The generation of both synthetic particles and firebrand digital models is detailed in the following sub-sections.

2.2.1. Generation of Synthetic Particles Synthetic particles were created by generating 3D point clouds within virtual boxes whose shapes conform to the shape

Table 3
Generation Parameters for Synthetic Particles Produced in the Present Study

Particle Class	Abbr.	Generated particle box dimensions min–max (cm)	Class limits	Particle max. projected area min–max (cm²)
I Equant	E	L_p: 0.4 to 13.7; I_p: 0.3 to 11.2; S_p: 0.2 to 10.9	$S_p/I_p > 1/2$ $I_p/L_p > 2/3$	0.1 to 130
II Rod				
Straight	RS	L_p: 0.5 to 14.6; I_p: 0.08 to 9; S_p: 0.05 to 8	$S_p/I_p > 1/2$	0.08 to 126
Bent	RB	φ: 18.7 to 180; R: 0.7 to 30 → L_p: 0.8 to 30; I_p: 0.07 to 8.8; S_p: 0.05 to 8	$I_p/L_p < 2/3$	0.11 to 129
III Blade				
Straight	BS	L_p: 0.5 to 14.6; I_p: 0.1 to 9.2; S_p: 0.05 to 3.7	$S_p/I_p < 1/2$	0.1 to 130
Bent	BB	φ: 18 to 180; R: 0.7 to 30 → L_p: 0.5 to 30; I_p: 0.24 to 9.7; S_p: 0.06 to 4.5	$I_p/L_p < 2/3$	0.13 to 128
IV Plate				
Straight	PS	L_p: 0.4 to 13.7; I_p: 0.3 to 11.3; S_p: 0.08 to 5	$S_p/I_p < 1/2$	0.1 to 129
Bent	PB	φ: 18 to 180; R: 0.3 to 30 → L_p: 0.4 to 16.1; I_p: 0.3 to 13.7; S_p: 0.05 to 5.2	$I_p/L_p > 2/3$	0.11 to 128

Abbr. Abbreviation

categories identified in Sect. 2.1 (*Equant*, *Rod*, *Blade*, and *Plate*). Point cloud density was set to be a function of particle volume and varied between 64,000 points/cm³ and 64 points/cm³ for the smallest ($\approx$ 0.006 cm³) and largest ($\approx$ 1367 cm³) box, respectively. Box dimensions L_p, I_p and S_p were randomized to ensure maximum aspect ratio coverage within each shape class. Class delineation followed a 2/3 threshold criterion for elongation (I_p/L_p) and 1/2 threshold criterion for flatness (S_p/I_p). The latter criterion differs from the one used in the original work of Zingg [45], but generally seems to offer better consistency with the shape class perception by a visual observer. Except for the *Equant* class, all classes were subdivided in two sub-groups, respectively containing convex ("straight") and non-convex ("bent") particles. Examples of particles populating each class are given in Fig. 1. For non-convex particles, L_p is governed by a set of two parameters, the angle φ and the radius of curvature R, both being randomized. A summary of the dimensional characteristics of the synthetized particle sets is provided in Table 3. Table 3 also features ranges for the corresponding particle maximum projected areas, which vary between 0.08 cm² and 130 cm². A total number of 7000 synthetic particles (1000 per sub-group) was produced to support the development of the shape classification model. Once generated, point clouds were converted into triangulated surface meshes to facilitate particle voxelization. All particle mesh files were tagged with their a priori known shape class. The synthetic particle gen-

eration process described above is designed to focus on firebrand macro-morphology, hence the reproduction of meso- (firebrand cracks) and micro- (firebrand fine texture/rugosity) shape irregularities is factored out in this work.

2.2.2. Generation of Firebrand 3D Digital Models Using 3D-Scanning Firebrand samples digitized in this work represent a small subset of a large firebrand population collected during a series of laboratory tests involving the combustion of small trees ($\approx$ 1.85 m average height) in the absence of wind [73]. In those tests, tree species (Balsam, Douglas, and Fraser firs), tree size/initial mass and tree moisture content were varied. The particle subset selected here essentially contained branches, twigs, needles, and small branch/twig junctions, with shapes representative of the majority of the particles contained in the collected pools. As bark-derived firebrands are typically not produced under low fire intensity and no wind conditions, the firebrand sample population was complemented with (unburned) bark pieces detached from oak trees collected on the National Institute of Standards and Technology (NIST) Gaithersburg campus during the fall season. These pieces are believed to be representative of larger combusted bark samples collected in field studies (e.g., [31]). Some pieces with strong curvature were included in this set (see side views for batch 5 in "Appendix 1"). Gathering both burned and unburned particle sets, a total number of 62 particles was 3D-digitized. Pictures of all particles, organized in batches, can be found in the "Appendix 1" along with the corresponding 3D mesh sample images. It is important to note that this set includes a wide range of firebrand shapes, some departing from the generic shapes described in the previous section, for instance, with non-constant cross-section along length (e.g., B4-4, B5-13), non-constant curvature (e.g., B1-2, B3-12) and presence of ramification (e.g., B1-11, B4-1).

In this work, all particles were digitized using a handheld structured-light scanner (*Space Spider*, *Artec 3D*) with nominal 3D resolution and 3D point accuracy up to 0.1 mm and 0.05 mm, respectively. The scanner allows for the digitization of small objects at working distances ranging from $\approx$ 0.2 m to $\approx$ 0.3 m, with maximum linear field of view dimensions 0.18 m $\times$ 0.14 m. Prior to scanning, particles were lightly pinned at the tip of a small fixture equipped with a fine needle (0.9 mm diam., inserted cross section $<$ 0.2 mm^2) and the fixture was placed at the center of an automated turntable (*Artec Turntable*, *Artec 3D*), see layout shown in Fig. 2a. Scans were performed by slowly moving the scanner in a single plane, the rotation of the firebrand being controlled by the turntable, itself automatically operated by the data acquisition software (*Artec Suite 17*, *Artec 3D*). The present setup allowed scanning operations in a single sequence, thus avoiding firebrand manipulation and software-based multi-scan alignments, found detrimental to the overall scanning fidelity (especially in the case of small size firebrands). Scanned frames were then processed within the data acquisition suite following a series of automated steps detailed in Fig. 3. Models obtained in the last step were then processed for firebrand fixture removal, the final output being in the form of watertight mesh (stereolithography format, STL), see example shown in Fig. 2b. For the 62 particles digitized in this work, the total number of faces per mesh and average mesh resolution varied from 6240 to $\approx$ 347,500 and from 0.2 mm to
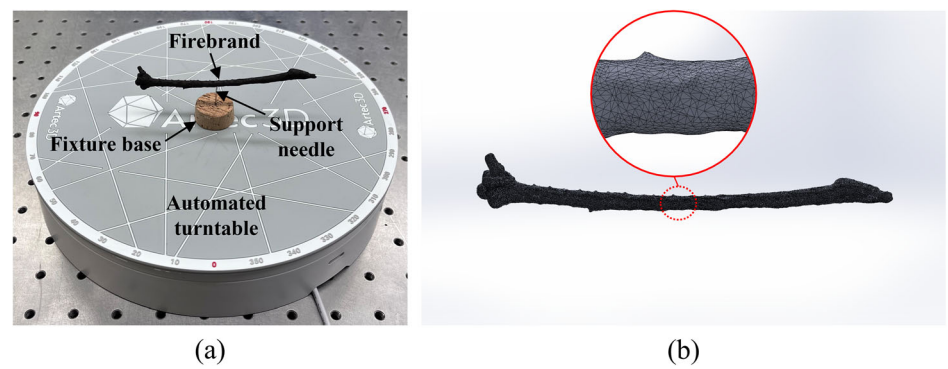
(a)   (b)

Figure 2.   Firebrand 3D scanning: (a) setup, and (b) example of output mesh model.
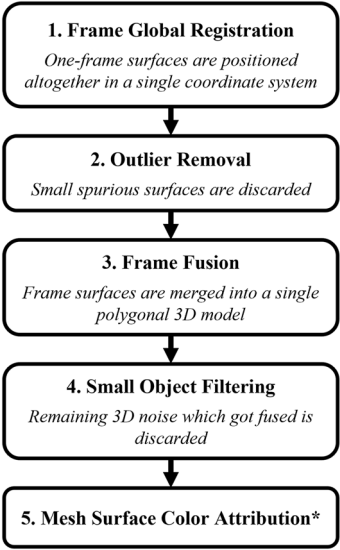

Figure 3.   Processing step flowchart for the 3D-scanned frames (*color information is used as part of the global registration process in step 1, but is not further used in the analysis that follows).

$\approx$ 0.56 mm, respectively. It is estimated that the entire scanning process (from sample preparation to creation of a digital model STL file) did not exceed 5 min per particle. All computerized scanning procedures were performed on a 16-core platform (Intel(R) Core(TM) i7-12850HX CPU) with 64 GB RAM and equipped with a NVIDIA GeForce RTX 3080 Ti (16 GB) GPU. All firebrand digital models (and associated measurements) are provided as Supplemental Material.
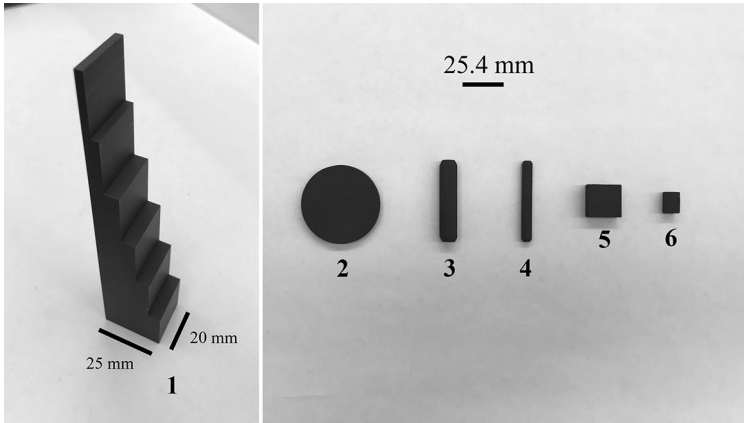
Figure 4. 3D scanning reference targets: (1) 6-step thickness calibration block, (2) disc, (3) large stick, (4) thin stick, (5) large cuboid and (6) small cuboid. Characteristic dimensions are provided in Table 4.

To verify that the approach detailed above provides reasonable accuracy, a set of reference targets was 3D scanned and some target characteristics extracted from the mesh models were compared to their known values (caliper measurements). These targets are shown in Fig. 4 and consist of: (1) a stainless steel 6 step calibration block (manufacturer thickness specifications 2.5 mm, 5 mm and 10 mm [+ 0.0 mm, − 0.02 mm] for the first three steps and 15 mm, 20 mm and 25 mm ([+ 0.0 mm, − 0.1 mm] for the last three steps); (2) a series of wooden particles including a large disc, two sticks with different diameters and two cuboids with different form factors. All objects were lightly coated in black using an ultra-matte charcoal color paint in order to match firebrand surface color appearance. Target dimension comparisons are provided in Table 4. For all wooden particles, dimensional errors were found to be low and contained within the − 1.3%, + 0.5% range. Errors for the calibration block were found to be noticeably higher, the maximum error nearing − 6% for the smallest step (2.5 mm). While flat surfaces are known to constitute a challenge for the 3D scanning process, especially at the frame registration level, it is interesting to note that the dimension of the calibration block second step (5 mm) is comparable to the thickness of the wooden disk (6.1 mm) but bears an error approximately 5 times higher. This would tend to indicate that the difference is primarily due to the particle surface optical properties rather than geometry (i.e., difference in reflective properties of lightly coated wooden/metal surfaces).

2.2.3. Measurements: Particle Data Format and Particle Voxelization As outlined above, all particle 3D models were initially generated in the form of triangulated surface meshes (STL file). Measurements were performed on point cloud (mesh vertices) and voxelized solid representations of the particles, derived from the mesh files. An illustration of all particle formats is provided in Fig. 5. Particle

Table 4
Actual Reference Target Dimensions (Caliper Measurements) Versus 3D Model Dimensions

Target	Dimension	Caliper measurements (mm)	From mesh file (3D scan) (mm)	Error (in %)
1. Calibration block	Step 1 (2.5 mm)	2.53 ± 0.01	2.38 ± 0.06	− 5.8
	Step 2 (5.0 mm)	5.04 ± 0.01	4.80 ± 0.07	− 4.8
	Step 3 (10.0 mm)	10.04 ± 0.01	9.73 ± 0.09	− 3.1
	Step 4 (15.0 mm)	15.02 ± 0.01	14.67 ± 0.05	− 2.3
	Step 5 (20.0 mm)	20.02 ± 0.01	19.64 ± 0.06	− 1.9
	Step 6 (25.0 mm)	25.03 ± 0.01	24.62 ± 0.03	− 1.6
2. Disc	Diameter	49.0 ± 0.27	49.15 ± 0.04	0.3
	Thickness	6.13 ± 0.05	6.07 ± 0.16	− 1.0
3. Large stick	Length	50.93 ± 0.10	50.86 ± 0.40	− 0.1
	Diameter	10.93 ± 0.06	10.99 ± 0.11	0.5
4. Thin stick	Length	50.42 ± 0.02	50.52 ± 0.17	0.2
	Diameter	6.41 ± 0.08	6.38 ± 0.13	− 0.4
5. Large cuboid	Side 1	20.0 ± 0.02	19.89 ± 0.12	− 0.5
	Side 2	19.81 ± 0.03	19.74 ± 0.10	− 0.4
	Thickness	9.74 ± 0.04	9.73 ± 0.11	− 0.1
6. Small cuboid	Height	13.0 ± 0.03	12.94 ± 0.13	− 0.5
	Side 1	8.1 ± 0.04	8.0 ± 0.11	− 1.3
	Side 2	7.79 ± 0.03	7.74 ± 0.06	− 0.6

Target geometries are shown in Fig. 4

mesh voxelization follows the work of Aitkenhead [74]. To ensure proper particle discretization while preserving computational tractability, voxel size S_v was initially set to 1/20th of the particle minimum bounding box (MBB) smallest dimension S, and the total number of voxels T_v forming the 3D shape was evaluated. If $(1 \times 10^6 \text{ voxels}) < T_v < (300 \times 10^6 \text{ voxels})$, the code proceeded to the evaluation of the particle maximum local thickness by fitting the largest sphere possible within the particle 3D boundaries. If the diameter of the sphere D_{ins} was found to be smaller than S, the voxel size was re-adjusted so that $S_v = D_{ins}/20$. Measurements were then performed on the resulting solid, and all particle descriptors detailed in the next section were computed. For the synthetic particles described above, T_v varies from 1×10^6 voxels to 60.5×10^6 voxels with S_v in the range 1.25×10^{-2} mm (particle with $L \times I \times S = 12.5$ mm $\times$ 0.75 mm $\times$ 0.25 mm) to 1.09 mm (particle with $L \times I \times S = 117.25$ mm $\times$ 110.25 mm $\times$ 105 mm).

2.3. Particle Descriptors: Choice and Definition

A list of the particle descriptors considered in the present study is provided in Table 5. The list contains general descriptors/measures, which correspond to particle characteristics directly evaluated on the particle 3D models, as well as shape-oriented descriptors, built as a combination of some of the particle characteristics. Not all descriptors are used in the statistical analysis described in Sect. 2.4; however, the full list constitutes a comprehensive set of entries for a database focused
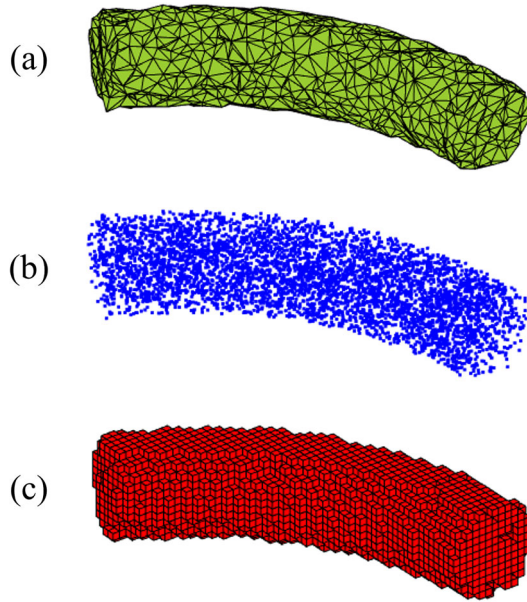
Figure 5. Particle formats: (a) stereolithography (STL) mesh, (b) point cloud, and (c) voxelized solid (voxel resolution decreased for illustration purposes).

on firebrand morphology that may be expanded in the future as needed. Unless otherwise mentioned, all descriptors were evaluated using the voxelized models of the particles. Additional details are provided below:

2.3.1. Minimum Bounding Box (MBB) Dimensions (L, I, S), Elongation (E_l), Flatness (F) and Equancy (E_q) L, I and S particle dimensions were extracted following the minimum bounding box (MBB) concept described by Blott and Pye [49], as implemented by Korsawe [75] (volume minimization approach). As alluded earlier, those dimensions correspond to the edge lengths of the smallest imaginary box that can contain the particle. The particle mesh vertices extracted from the particle mesh files served as point cloud inputs for the calculations. Particle elongation E_l (formula: I/L), flatness F (formula: S/I), and equancy E_q (formula: S/L), were derived using the MBB dimensions, following already established conventions [49]. Note that for ideal particles (e.g., cylinders, discs), similar formulations have been used to define a firebrand *aspect ratio* as a mean for categorization in the context of aerodynamic studies, see for instance the work of Tohidi et al. [10].

2.3.2. Volume (V), Surface Area (SA), and Sphericity (S_{ph}) The particle volume V was obtained by summing all elemental voxels forming the 3D shape. The particle surface area SA was computed following the method developed by Lehmann and Legland [76], which leverages the Crofton formula to measure perimeter/sur-

Table 5
Summary of the Particle Descriptors Considered in the Present Work (MBB: Minimum Bounding Box)

Parameter	Symbol/Formula	Range	PCA	Notes
General descriptors/measures				
Particle MBB dimensions	L, I, S	> 0	X	Dimensions of the smallest imaginary box that can contain the particle
Volume	V	> 0	X	Particle volume (sum of elemental voxels)
Surface area	SA	> 0	X	Particle surface area
Maximum projected area	MPA	> 0	X	Max. of particle projected areas (following the MBB edge directions)
Geodesic length	L_g	> 0	X	Length of the shortest 3D path that can be drawn, within the 3D shape, between known particle extremities
Largest inscribed sphere diameter	D_{ins}	> 0	X	Diameter of the largest sphere that can be contained within the particle 3D boundaries
Moments of inertia	$\alpha_1, \alpha_2, \alpha_3$	0:0.5	✔	Normalized particle moments of inertia, $\alpha 1 + \alpha 2 + \alpha 3 = 1$ and $\alpha 1 \geq \alpha 2 \geq \alpha 3$
Shape descriptors				
Elongation	$E_l = I/L$	0:1	✔	Characterizes the particle elongation using the MBB intermediate I and largest L dimensions
Flatness	$F = S/I$	0:1	✔	Characterizes the particle flatness using the MBB smallest S and intermediate I dimensions
Equancy	$E_q = S/L$	0:1	✔	Characterizes the particle equancy using the MBB smallest S and largest L dimensions
Sphericity	$S_{ph} = \sqrt[3]{36\pi V^2}/SA$	0:1	✔	Characterizes particle sphericity by comparing the surface area of an imaginary sphere with volume V to the particle surface area SA
Convexity	$C_x = V/V_{hull}$	0:1	✔	Characterizes the particle convexity by comparing the particle volume V to the volume V_{hull} of the particle convex hull
Compacity	$C_c = V/V_{MBB}$	0:1	✔	Characterizes the particle compacity by comparing the particle volume V to the volume V_{MBB} of the MBB
Geodesic elongation index	$E_g = L/L_g$	0:1	✔	Characterizes the particle true elongation by comparing the particle geodesic length L_g to the MBB largest dimension L
Maximum local thickness index	$T = D_{ins}/S$	0:1	✔	Characterizes the particle maximum local thickness by comparing the diameter D_{ins} of the particle largest inscribed sphere to the MBB smallest dimension S

The PCA column indicates which particle descriptors were selected in the initial pairwise correlation analysis (✔: selected, X: not selected). Descriptors kept in the final PCA are identified by the underlined tick marks (see related discussion in Sect. 3)
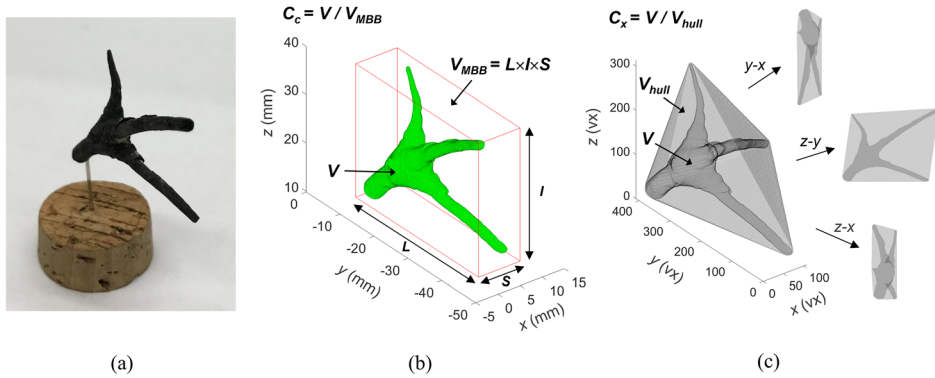
Figure 6. Illustration of the particle compacity and convexity definitions: (a) picture of firebrand B1-11 (see "Appendix 1"), (b) corresponding mesh file with surrounding minimum bounding box for particle compacity (C_c) evaluation (note that the volume V is extracted using the particle voxelized model), and (c) particle voxelized model with corresponding convex hull for particle convexity (C_x) evaluation (particle/hull projections following the three orthogonal directions set by the reference frame are shown to the right).

face of discretized objects. Particle sphericity S_{ph} (formula: $\sqrt[3]{36\pi V^2}/SA$) was calculated using both V and SA as specified above.

2.3.3. Maximum Projected Area (MPA) To ensure continuity with previous studies that essentially focused on the determination of firebrand cross-sectional areas, a maximum projected area *MPA* was computed for each particle. Each particle voxelized model was projected following the three orthogonal directions set by the particle MBB, and the largest projected area was retained.

2.3.4. Convexity (C_x) and Compacity (C_c) The convexity C_x (formula: V/V_{hull}) and compacity C_c (formula: V/V_{MBB}) were implemented to compare the particle volume V to the volume V_{hull} of its convex hull and to the volume V_{MBB} of the associated MBB, respectively. V_{hull} was computed as the smallest convex polygon that can contain the 3D shape. V_{MBB} was computed via the known MBB dimensions L, I and S. An illustration of both definitions is provided in Fig. 6.

2.3.5. Geodesic Length (L_g) and Geodesic Elongation Index (E_g) As alluded in Sect. 2.1, non-convex particles may not be properly classified solely based on their MBB dimensions. An example where such a characterization would fail is given in Fig. 7a. Using the MBB dimensions and standard classification diagrams (e.g., Zingg [45]), the non-convex twig shown in Fig. 7a would be classified as a bladed particle (see MBB footprint in Fig. 7b). Clearly, descriptors able to unravel complex 3D morphological attributes need to be employed. To this end, we introduced the particle geodesic length L_g; L_g represents the length of the shortest path
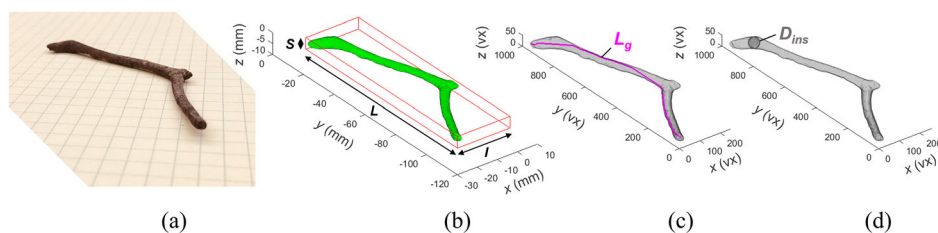
Figure 7. Example of a firebrand (see B1-2 in "Appendix 1") for which traditional shape classification methods would fail: (a) firebrand picture, (b) firebrand 3D model (mesh representation) with surrounding minimum bounding box and corresponding dimensions *L*, *I* and *S*, (c) voxelized model of the firebrand showing the computed particle geodesic length *L_g* (magenta line shows the particle inner path), and (d) voxelized model of the firebrand showing the computed maximum inscribed sphere with diameter *D_ins* (Color figure online).

that can be drawn, within the 3D shape, between the known particle extremities (see illustration in Fig. 7c). For particles with intricate shapes, L_g is a more suitable metric for meaningful elongation characterization [48, 58, 59]. In the present work, the computation of the geodesic length is based on the developments made by Legland [77]. It is incorporated in the geodesic elongation index E_g (formula: L/L_g) that compares the particle MBB largest dimension L to the particle geodesic length L_g.

2.3.6. Largest Inscribed Sphere Diameter (D_{ins}) and Maximum Local Thickness Index (T) By the same token, the MBB dimension S may not be representative of the actual particle thickness (e.g., twisting the particle shown in Fig. 7a would result in a dimension S much larger than the particle actual thickness). We thus retained D_{ins}, introduced earlier as the diameter of the particle largest inscribed sphere, as relevant descriptor to characterize the size of the particle core (see example shown in Fig. 7d). It is incorporated in the maximum local thickness index T (formula: D_{ins}/S), which compares D_{ins} to the particle MBB smallest dimension S.

2.3.7. Moments of Inertia (α_i) Assuming uniform mass distribution (identical weight of all elemental voxels), the moments of inertia of a particle will depend on its shape/3D spatial arrangement [58]. Here, we followed the approach described by Parra-Denis [66] by first computing the particle principal moments of inertia I_i, which were then normalized so that $\alpha_i = I_i/(I_1 + I_2 + I_3)$, $i = 1, 2, 3$. Additional details regarding the calculations of the principal moments of inertia are provided in the "Appendix 2".

Because all particle models are processed in the discretized form, measurement errors are inevitable. These errors essentially depend on the voxel resolution, the

particle shape and the particle measure considered. It is possible to gain a better understanding of the measurement errors involved via the use of ideal particles for which measures are known beforehand. To achieve this, a set of particles with common characteristic dimensions δ = 25.4 mm and τ = 5 mm was generated using Computer-Aided Design (CAD) tools, and measurements performed by the algorithms in place were compared to the known values. These particles include: a cube (side length: δ), a disk (diameter: δ, thickness: τ), a plate (side length: δ, thickness: τ), a round rod (length: δ, diameter: τ) and a sphere (diameter: δ). Given the particle voxelization procedure highlighted earlier, the measurement relative errors were in the range $(-0.4 \text{ to } 0.0)\%$ for the MBB dimensions L, I and S, $(0.0 \text{ to } 0.9)\%$ for the volume V, $(-7.9 \text{ to } 0.6)\%$ for the surface area SA (consistent with observations reported in [76]), $(-4.7 \text{ to } 14.1)\%$ for the geodesic length L_g, and $(-1.5 \text{ to } 0.0)\%$ for the largest inscribed sphere diameter D_{ins}.

2.4. *Principal Component Analysis*

Principal Component Analysis (PCA) is a statistical method that allows high-dimensional datasets to be visualized and studied in a lower dimensional space while preserving maximum data variability. Typically, the technique leverages a new set of coordinates that can be used to represent the data without sacrificing too much information. Each new coordinate, referred to as Principal Component (PC), is a linear combination of the problem original variables. PCs are identified by successively finding directions along which the dataset retains maximum variance. All PCs are defined orthogonal; hence they are uncorrelated. The reader is referred to the literature for both basic [78, 79] and advanced coverages [80, 81] of the topic. PCA is used in a wide variety of fields such as genetics, computer vision, or finance, to cite a few.

PCA is often applied to unsupervised classification problems for which classes of elements forming a population are not known beforehand. Hence, it is usually followed by a classification step that involves some sort of grouping technique, the most popular being hierarchical or K-means clustering analyses [82]. In the present case, PCA is applied to the synthetic particle dataset, thus the class of each element is known a priori (class limits were set initially, see Sect. 2.2 and Table 3). PCA is essentially used to provide convenient graphical representation of the data to help visualize the degree of separation between the known groups [80], and ultimately, assess the need for additional discriminant rules. Provided that proper separation between groups is obtained, the synthetic particle PCA can be used to classify brand new elements by comparing their 3D location (in the PCA space) to the 3D arrangements of the known shape clusters.

In this work, the PCA analysis is performed on the synthetic particle dataset using MATLAB [83]. The PCA input variables are selected among the list of the particle descriptors detailed previously (see discussion in the next section regarding the selection process). Prior to the analysis, the data is centered and standardized. The singular value decomposition (SVD) algorithm is used. The focus is set on the first three principal components (which accounted for 93.4% of the data variance) to allow for easy visualization of the data clusters in 3D space by preserving both maximum data

variability and graphical legibility. In what follows, the firebrand digital model samples are projected in the PCA space of the synthetic particles. To do so, the digital model descriptors are centered and standardized according to the statistical characteristics of the synthetic particle population. Once projected in the PCA space, the classification is performed by identifying the shape class of the digital model's three closest neighbors, and the digital model's shape is labeled accordingly.

3. Results

Particle descriptors initially considered are highlighted in the Table 5 (see tick mark in the PCA column): these include the conventional elongation, flatness and equancy descriptors, the particle sphericity, convexity and compacity and the new indices based on the particle geodesic elongation and maximum local thickness. The particle normalized first two moments of inertia are included as well. Prior to applying the PCA to the synthetic dataset, a descriptor pairwise correlation analysis is performed to help reduce the number of input variables. The results are shown in Fig. 8 for which both point clouds and Pearson's correlation coefficients are provided. The particle compacity C_c is found to be positively correlated with the particle convexity C_x ($r = 0.97$). Similarly, the particle normalized moments of inertia α_1 and α_2 show strong negative correlation with the particle equancy E_q ($r = -0.96$) and elongation E_l ($r = -0.97$), respectively. Hence, C_c, α_1 and α_2 are not further considered in the analysis.[2] Interestingly, the geodesic elongation index E_g displays strong negative correlation with the particle elongation E_l ($r = -0.89$), likely a manifestation of the simple constant 2D curvature model adopted in this work (for a known particle shape and a fixed geodesic length L_g, L and I measures directly depend on particle curvature, and both measures form the basis for elongation index formulations). For the sake of computational simplicity, we remove E_g from the list of the PCA inputs in what follows, bearing in mind that the correlation might not hold for particle characterized by complex 3D curvature (hence, the inclusion of E_g needs to be reassessed should more intricate geometries/shapes be considered in the future).

The PCA for the synthetic particle dataset is shown in Fig. 9 (input variables: E_l, F, E_q, S_{ph}, C_x and T). An animated view of the plot is provided as Supplemental Material for enhanced legibility. The different particle shape clusters are found to occupy distinct sub-volumes in the 3D PCA space with minimal spatial overlap. Clusters for convex shape categories (E, PS, BS, RS) seem to fit together as a 3D dimensional surface while clusters for non-convex shapes (from top to bottom: PB, BB, RB) form adjacent clouds that extend away from the 3D surface (see "Convex" and "Non-convex" highlights in the insert of Fig. 9, respectively). These clouds typically display a higher degree of scatter as compared to their convex counterpart. As the principal component axes may correlate with the selected shape descriptors to various extent, the principal component coefficients can help better describe major trends in shape transitions along the PCA axes. The coef-

---

[2] C_x is chosen over C_c due to its established use throughout the particle morphology literature, while E_q and E_l are selected over α_1 and α_2 for the sake of computational simplicity.
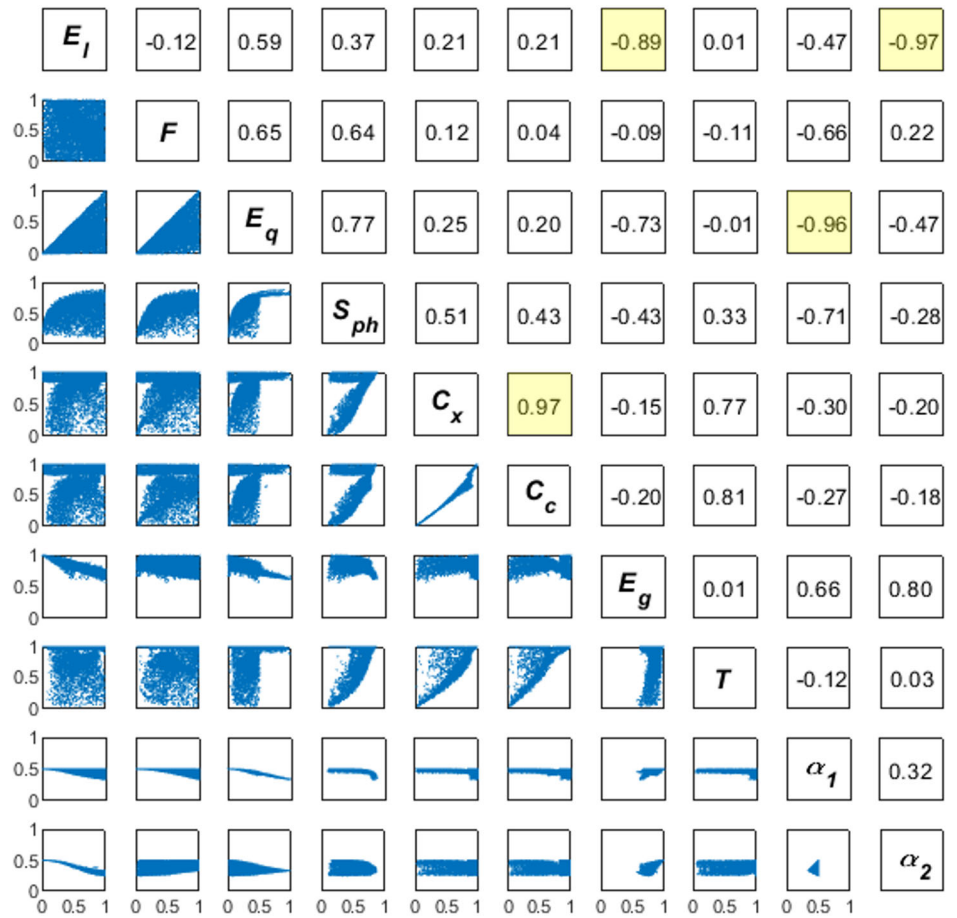
Figure 8. Particle descriptors pairwise correlation analysis (numbers indicate corresponding Pearson's correlation coefficients). The yellow highlights indicate descriptor pairs with high correlation (Color figure online).

ficients are provided in Table 6. PC1 is found to be primarily correlated with E_q and S_{ph}, hence descending PC1 values will tend to indicate a departure from the equant class (higher PC1 values) towards other shape categories (lower PC1 values). PC2 displays strong positive correlation with C_x and T, and thus may be seen as a marker for particle change of convexity/curvature. PC3 is highly positively correlated with E_l, and negatively correlated with F, hence provides information on shape transition between plate (higher PC3 values) and rod (lower PC3 values) categories. Overall, the clear separation between the different shape groups warrants further use as classification tool following the approach detailed in the previous section.

The firebrand digital model dataset is projected into the synthetic particle 3D PCA space (see black crosses in Fig. 9) and the shape category of each firebrand
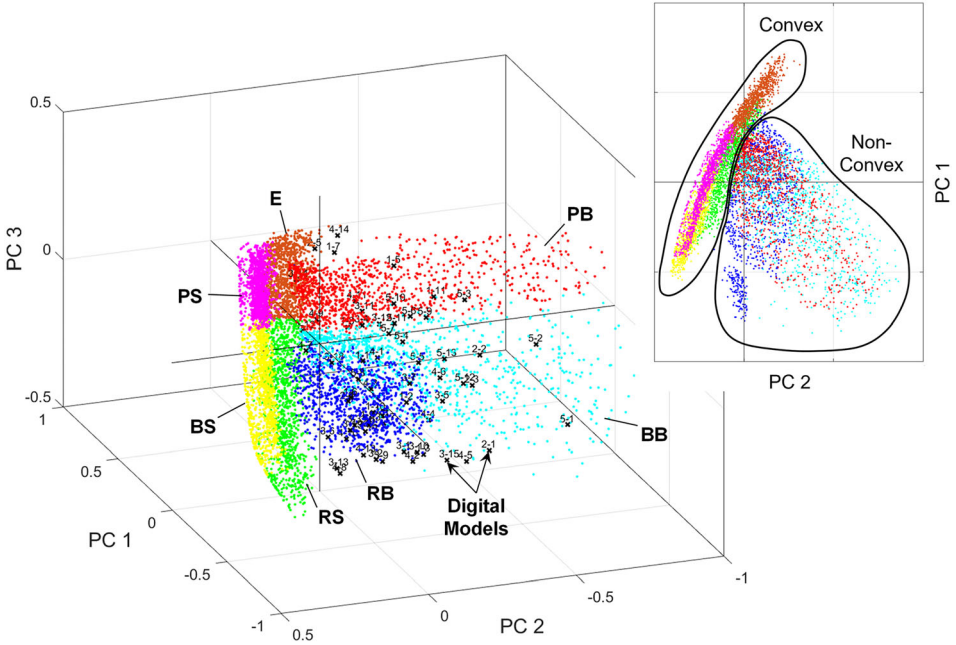
Figure 9. Particle synthetic dataset plotted in the PCA space (input variables: E_l, F, E_q, S_{ph}, C_x and T). Symbol color correspond to the different shape categories defined in Table 3: E - Equant (brown), RS - Rod Straight (green), RB - Rod Bent (dark blue), BS - Blade Straight (yellow), BB - Blade Bent (cyan), PS - Plate Straight (pink), PB - Plate Bent (red). Crosses (black) with identifiers: projected firebrand digital models. Upper right insert: top view of datapoint cloud with convex/non-convex particle cluster identification (Color figure online).

Table 6
Correlation Matrix Between the PCA Axes and the Shape Descriptors (the Table Indicates the Corresponding Principal Component Coefficients)

	PC1	PC2	PC3
E_l	0.2990	−0.0781	0.8034
F	0.3666	−0.3868	−0.5521
E_q	0.5132	−0.3267	0.1430
S_{ph}	0.5562	−0.0551	−0.1094
C_x	0.3838	0.5318	−0.0588
T	0.2371	0.6721	−0.1173

is inferred from its three closest synthetic neighbors. To use the maximum available information and possibly remove any ambiguity, the PCA first four components are used in the distance computations. The results of the classification
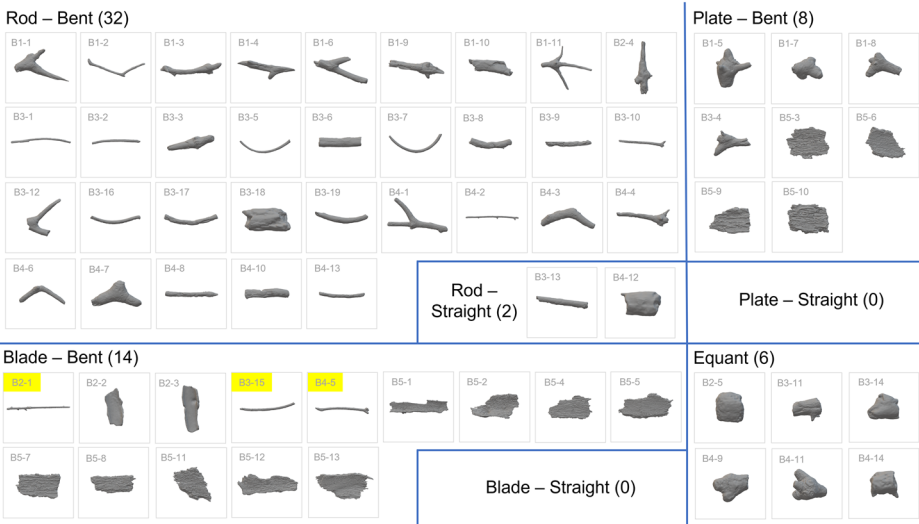
Figure 10. **Firebrand classification results (firebrand images not to scale). Yellow highlights indicate firebrands likely to be classified in a different category based on simple visual observation (Color figure online).**

are shown in Fig. 10. The Rod categories (Bent/Straight) regroup the quasi-totality of the firebrands made of twigs and branches, including the more challenging ramified shapes (particles B1-11 and B4-1). Notable exceptions, not included in this category but visually displaying rod-like features, are firebrands B2-1, B3-15 and B4-5 classified as non-convex blades (see yellow highlight in Fig. 10). A closer look at the corresponding digital models reveals that the misclassification is due to complex morphological features that were not considered while generating the synthetic particle set. These features are highlighted in Fig. 11. Non-constant cross-section (protruding volumes due to broken ramifications, see firebrand B2-1, Fig. 11a) and pronounced 3D curvature (see firebrand B3-15, Fig. 11b) contribute to an increase of the MBB dimension S. As a result, S significantly departs from the firebrand core dimension D_{ins}. This difference is believed to be a driving factor leading to blade identification given the rather simple firebrand synthetic geometries. Note here that convexity values extracted from the digital models and their closest synthetic neighbors are similar ($C_x = 0.23$ and 0.36 for B2-1 and B3-15 respectively, vs. $C_x = 0.29$ and 0.42 for their synthetic counterparts), hence suggesting that it cannot be used as a discriminant factor in these specific cases (for further details, see the descriptor set comparison provided in the "Appendix 3"). Particle B4-5, not shown in Fig. 11, likely suffers from both effects mentioned above. The Blade (Bent) category is otherwise populated by the long bark pieces found in batch #5 as well as small blady particles (likely from delaminated burned branches, see particles B2-2 and B2-3). As expected, the Equant category gathers the small compact firebrands found across batches #2, #3 and #4. Although properly classified, firebrands B3-11 and B4-11 are situated slightly away from the con-
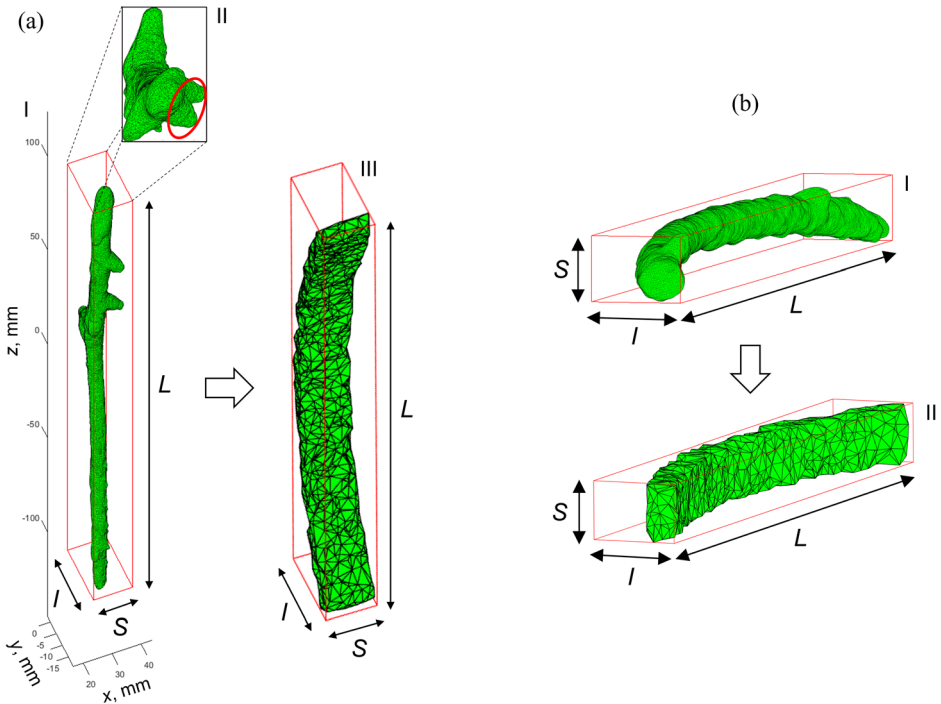
Figure 11. Illustration of firebrand misclassification: (a) Firebrand B2-1—I. digital model with MBB; II. top view showing bulges contributing to S increase; III. corresponding closest synthetic neighbor with MBB. (b) Firebrand B3-15—I. digital model with bounding box showing 3D curvature; II. corresponding closest synthetic neighbor with MBB (models not to scale). See "Appendix 3" for additional details.

vex particle surface highlighted in Fig. 9, a manifestation of lower firebrand convexity values ($C_x = 0.74$ and 0.76, respectively) as compared to the averaged C_x value for the equant synthetic set (0.95). Finally, the non-convex Plate (Bent) category is made of two subgroups with distinct morphologies: the platy bark pieces from batch #5 and the small twig/branch junctions from batch #1 and #3. While the former type can be easily confirmed as belonging to the non-convex (bent) plate category upon simple visual observation, the second type offers more challenges for direct visual verification as they depart from the ideal categories established, primarily due to their complex 3D non-convex nature. These particles do, however, share descriptors that are consistent with those extracted for small, curved plates, which differ from typical equant particle values (e.g., MBB dimension S markedly smaller than the two other ones, convexity and sphericity values away from 1.0, etc.). Hence, it is believed that these particles are best suited in the non-convex (bent) plate category (as compared to any other existing category).

4. Discussion and Additional Considerations

Overall, Fig. 10 shows that the classification methodology proposed performs reasonably well despite the simplicity of the synthetic particle base geometries. Hence, the framework established offers an efficient way to better understand firebrand morphology, with the following advantages:

(1) The proposed approach solely relies on extraction of measurable features of the digitized particles which removes possible classification ambiguities (and potentially bias/subjectivity should the task be manually/visually performed) and hence, offers a robust framework for firebrand population morphology documentation and comparison. Additionally, the use of digital models permits evaluation of some particle characteristics that would be otherwise difficult (if not impossible) to physically measure (e.g., surface area, geodesic length, etc.) given the shape complexity and fragility of the firebrand specimen involved.

(2) Once the classification step has been completed, particle statistics can be retrieved by shape category. This is essential for reporting particle dimensions as the meaningful information may differ depending on the shape class considered (e. g., dimensions of a bent rod may be represented by its core diameter D_{ins} and its geodesic length L_g, an equant by its averaged side length, etc.). As an illustration, distribution histograms for D_{ins}, L_g, V and MPA are provided in Fig. 12 for the bent rod population identified in Fig. 10. This type of information is expected to be instrumental to support modeling efforts devoted to reacting firebrand flows, by for instance allowing probability density functions describing distributions of the particle characteristics to be built. Note that the list of meaningful particle characteristics considered in Fig. 12 is arbitrary, and it can be expanded for and/ or tailored to a specific problem (e.g., including moments of inertia for firebrand aerodynamics-related problems, including a surface area offered for contact for ignition-related problems, etc.)

(3) The proposed approach can be performed in a time-efficient manner (see details in Sect. 2.2). While certainly not as rapid as the conventional firebrand projected area method, the amount of novel information acquired and the nature of the format in which it is delivered (STL files can be queried as needed and only require minimal storage space) largely outweigh the downsides of longer processing times. It also important to mention that novel 3D scanning technologies have emerged; these technologies now enable simultaneous 360° scanning of multiple objects without user intervention, possibly reaching a throughput of several hundred scanned specimen per day. This implies that batch scanning of firebrand sample populations may now be performed quickly without extensive firebrand manipulation. Using these technologies would considerably speed up the 3D scanning tasks outlined in this work, likely leaving most time-consuming operations to the firebrand generation and collection steps.

As discussed in the previous section, some limitations remain when real firebrand shapes significantly depart from the particle synthetic models, especially in the rod category where shape irregularities (non-constant cross-section) and complex 3D curvature effects may be present. While shape irregularities could be handled using additional processing steps (e.g., by applying erosion techniques to the
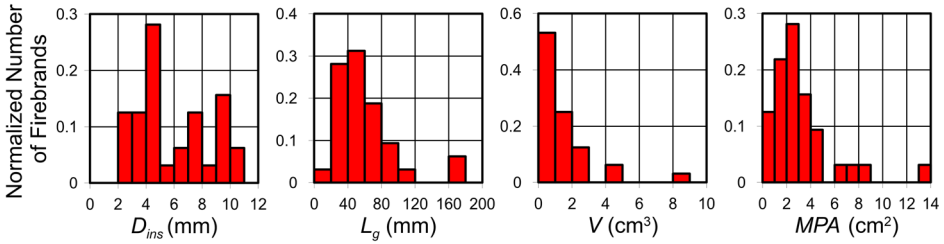
Figure 12. Characteristics of firebrands classified as bent rods (BR) in Fig. 10 (total number of particles: 32).

3D firebrand models to suppress bulges followed by shape classification of the resulting firebrand "cores"), 3D curvature effects may need to be incorporated in the generation of the synthetic particle models and the use of additional particle shape descriptors may need to be re-assessed accordingly (inclusion of the geodesic elongation index, development of a new descriptor quantification the extent of deviation from simple 2D curvature). Classification of ramified firebrands (B1-11, B4-1) in a separate shape category might also be desirable and remains to be investigated.

   From a methodological standpoint, it is important to remind that, given the significant amounts of firebrand generated during WUI fires and the wide disparity of sizes involved, digitizing all firebrands in a sample population may be precluded. In practice, it might be useful to define a size threshold below which firebrands will not be processed. There are different ways, however, as to how this threshold could be defined. Based on the 3D scanning procedure developed in this work, small firebrands with thicknesses below ≈ 1 mm were found rather challenging to scan (for instance, the thinnest firebrand considered in this study, firebrand B2-2, is ≈ 0.8 mm thick and required multiple trials for proper digitization). It might not be judicious to include firebrands that are too small in the present analysis, because: (1) for very small firebrands with almost negligible mass, shape is less of a governing parameter to understand particle aerodynamics, deposition behavior, etc.; (2) some of the smaller particles could be generated involuntarily during the collection, transport, and preparation of the firebrands (due to their relative fragility), and hence, introduce bias into the results. Should firebrands with thicknesses on the order of ≈ 1 mm be considered, it is recommended that their intermediate and largest dimensions span at least several millimeters (e.g., > 5 mm). From a purely practical standpoint, the threshold could be set by establishing a size cutoff considering a critical firebrand quantity that can be processed, ensuring that the entire analysis remains manageable (timewise/resourcewise). The downside of such an approach is that the threshold selected will be dependent on the nature of the experiment and the breadth of the data collected, which may not facilitate meaningful datasets comparisons across experiments. Finally, it might be desirable to select a size threshold relevant to the firebrand ignition problem. This would require a detailed understanding of ignition propensities of recipient fuels in the WUI versus firebrand size characteristics, which is

still a topic of active research. Note that in this case, particle size may not be the only relevant parameter to consider: particle physicochemical properties, and especially particle mass, would also be of interest, hence there is value in "augmenting" the firebrand digital models with such data (i.e., building firebrand digital models akin to digital twins).

Moving forward, the approach developed in this work could be used to structure a firebrand classification model based on digital model datasets of real firebrand populations (rather than synthetic particle models) to ensure that the widest range of firebrand morphology complexity is accounted for. Firebrand shape classes could be defined using PCA and unsupervised clustering analysis performed on a large number of datasets, collected for a wide range of field conditions (including various fuels, both vegetative and structural, wind conditions, etc.). Because such an effort may require extensive resources (thorough sample field collection and digitization), the authors strongly encourage collaborative work among the fire research community to fulfill this challenging goal.

Lastly, while the research highlighted in this work is geared towards supporting post-fire analysis of collected firebrand sample populations, the proposed classification model could be used to study airborne firebrand showers. Recently developed tools have demonstrated a potential for airborne firebrand shape reconstruction using multi-view imaging systems and the Visual Hull concept [67]. In this regard, the impact of spatial resolution (intrinsically limited in the case of consumer-grade cameras as compared to 3D scanning devices) and reconstruction artifacts (stemming from the limited number of views) warrants further investigations to understand how the classification approach developed in this work can be efficiently applied in this particular context.

5. Conclusion

From airborne particle generation to ignition of a recipient fuel, particle morphology is central to many firebrand-related problems. While previous studies have focused on firebrand projected area as sole metric for morphology characterization, the framework developed here intends to provide methods to classify and compare firebrand population shapes and sizes in a thorough and systematic manner via the use of multi-dimensional shape descriptors applied to 3D firebrand models. To do so, a large set of synthetic particles (7000 in total) was generated to form the backbone of a simple shape classification model. These synthetic particles, designed to share common features and measures with actual firebrands (overall shape, curvature, projected areas and when available, characteristic dimensions), could be categorized in four generic classes: equant, rod, blade, and plate. All of them, equant class aside, contained both convex ("straight") and non-convex ("bent") elements, the latter being affected by constant 2D curvature. Following a descriptor pairwise correlation analysis, Principal Component Analysis (PCA) was applied to the synthetic particle dataset with the following six 3D shape descriptors as input parameters: elongation, flatness, equancy, sphericity, convexity, and maximum local thickness index (ratio of the particle maximum

inscribed sphere diameter to the smallest dimension of the particle minimum bounding box). It was found that clear spatial delineation of the different shape clusters could be obtained in the PCA 3D space with the first three principal components as coordinates, hence permitting unambiguous shape identification based on 3D spatial location of a datapoint. A set of real firebrands (49 pieces in total) collected during tree burns (Balsam, Douglas firs), complemented with unburned bark pieces (Oak, 13 pieces), was 3D scanned and the resulting digital models were processed to extract the corresponding shape descriptors. The digital model population was then projected in the PCA space, and the model shape classes were inferred from the classes of the closest synthetic elements. Despite the shape complexity of the real firebrands (real shapes often depart from the ideal generic shapes for several reasons: e.g., because of non-constant cross section/bulges, non-constant curvature, ramifications, etc.), classification results were found to be very good overall. Noticeable misclassification occurred for few rod-like elements (3/37), and these were traced back to the influence of shape irregularities/bulges (along the direction of the particle minimum bounding box smallest dimension) and/or overall pronounced 3D curvature effects. Moving forward, the techniques implemented in this work will be used to structure a classification model based on real firebrand digital model populations and unsupervised shape clustering analyses. Application to airborne firebrand flow problems will also be considered.

Acknowledgements

Declarations

Conflict of interest   The authors declare that they have no known competing financial interests or personal relationships that could have appeared to influence the work reported in this paper.

Open Access

Appendix 1: 3D-Digitized Particles

See Figs. 13, 14, 15, 16, 17
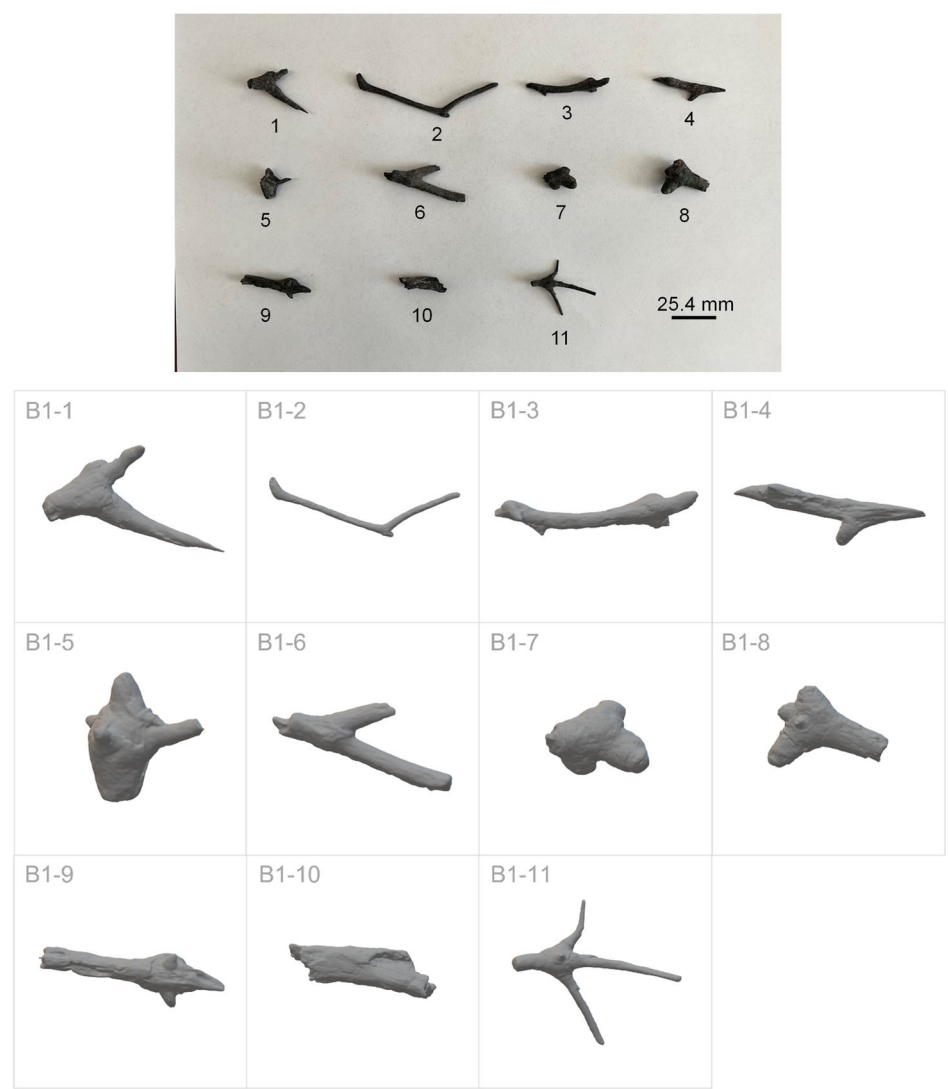
Figure 13. Firebrand samples — Batch #1 (Balsam Fir). Top: firebrand sample top view, Bottom: sample images of 3D digital models.

Figure 14.   Firebrand samples — Batch #2 (Douglas Fir). Top: firebrand sample top view, Bottom: sample images of 3D digital models.
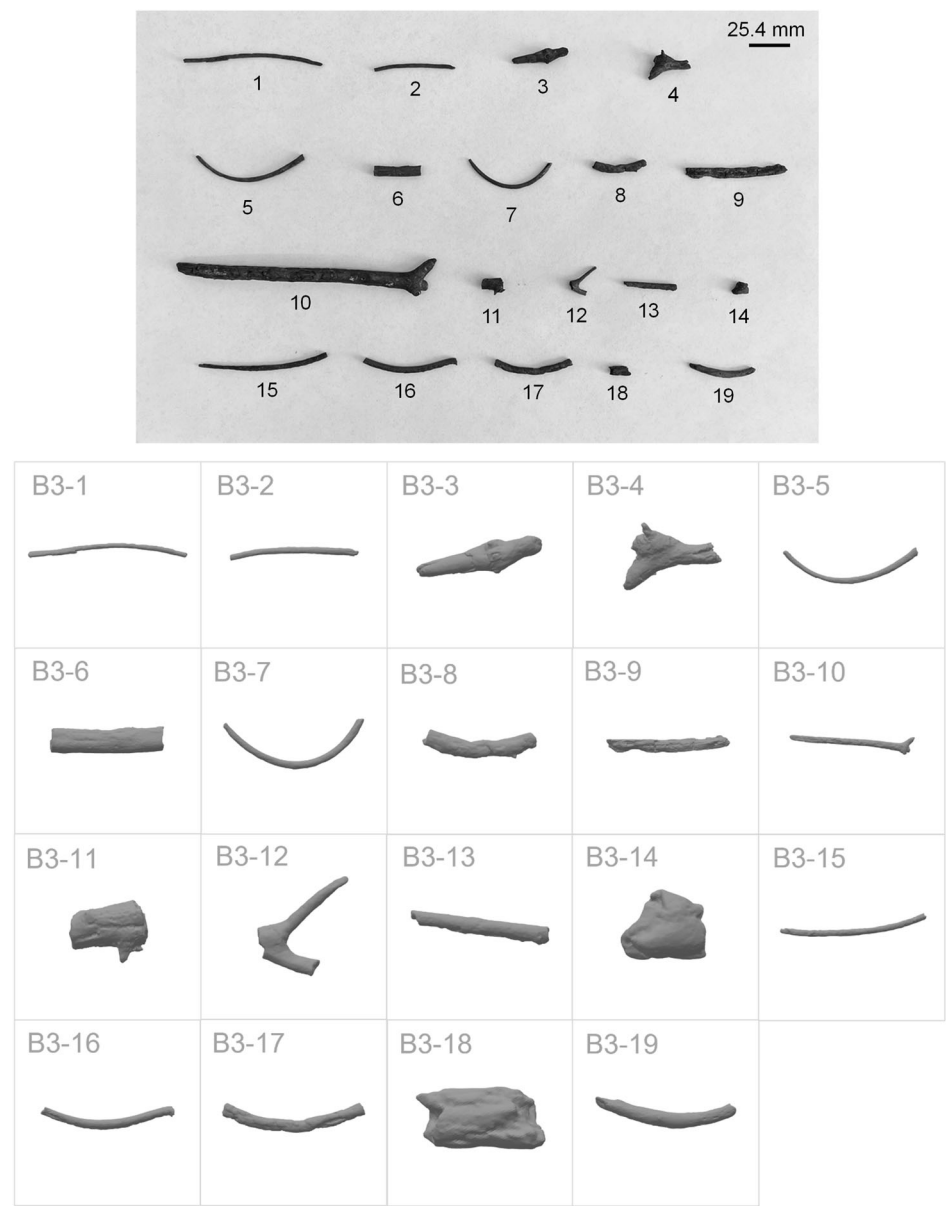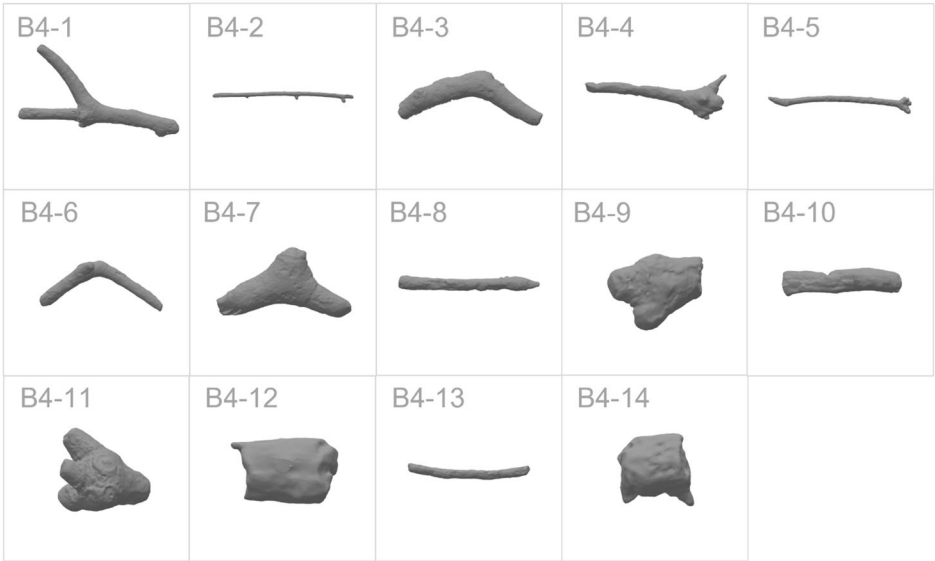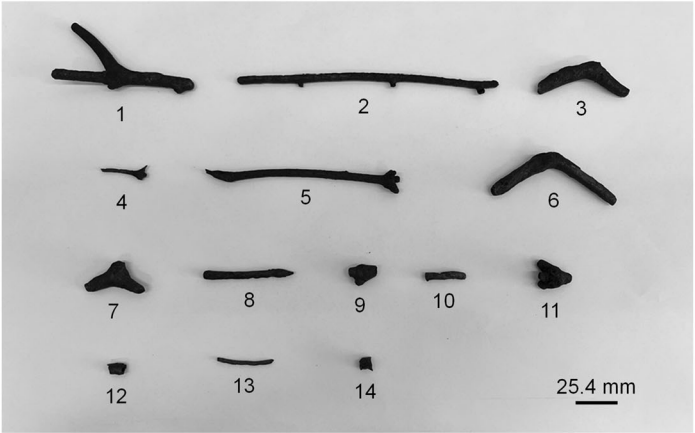
Figure 15. Firebrand samples — Batch #3 (Balsam Fir). Top: firebrand sample top view, Bottom: sample images of 3D digital models.

Figure 16.   Firebrand samples — Batch #4 (Balsam Fir). Top: firebrand sample top view, Bottom: sample images of 3D digital models.

Figure 17.   Firebrand samples — Batch #5 (Oak). Top: firebrand sample top view, Middle: firebrand sample side view (showing max. curvature), Bottom: sample images of 3D digital models.

Appendix 2: Calculation of Particle Principal Moments of Inertia

For a voxelized particle, the matrix of inertia I can be expressed as:

$$I = \begin{pmatrix} I_{xx} & -I_{xy} & -I_{xz} \\ -I_{yx} & I_{yy} & -I_{yz} \\ -I_{zx} & -I_{zy} & I_{zz} \end{pmatrix}. \tag{1}$$

With the products of inertia defined as:

$$I_{xy} = I_{yx} = \sum_i m_i x_i y_i, \tag{2}$$

$$I_{yz} = I_{zy} = \sum_i m_i y_i z_i,$$

$$I_{xz} = I_{zx} = \sum_i m_i x_i z_i,$$

and the moments of inertia defined as:

$$I_{xx} = \sum_i m_i \left(y_i^2 + z_i^2 \right), \tag{3}$$

$$I_{yy} = \sum_i m_i \left(x_i^2 + z_i^2 \right),$$

$$I_{zz} = \sum_i m_i \left(x_i^2 + y_i^2 \right),$$

where x_i, y_i, and z_i are the particle voxel coordinates in a reference frame centered on the particle center of inertia, with axes orientation matching those of the reference frame adopted for particle voxelization; m_i, the elemental mass, is taken here as unity, assuming uniform mass distribution throughout the particle.

In this work, the particle principal moments of inertia are extracted performing the following steps: (1) the particle center of inertia is computed; (2) the matrix of inertia I is computed using expressions B1, B2 and B3; (3) the principal moments of inertia I_1, I_2 and I_3 are found by diagonalizing the matrix of inertia I such as:

$$I = P \begin{pmatrix} I_1 & 0 & 0 \\ 0 & I_2 & 0 \\ 0 & 0 & I_3 \end{pmatrix} P^{-1} \tag{4}$$

with P an invertible matrix whose column vectors correspond to the particle principal axes of inertia.

Appendix 3: Particle Descriptor Comparison for Selected Misclassified and Correctly Classified Firebrand Digital Models

See Fig. 18 and Table 7.
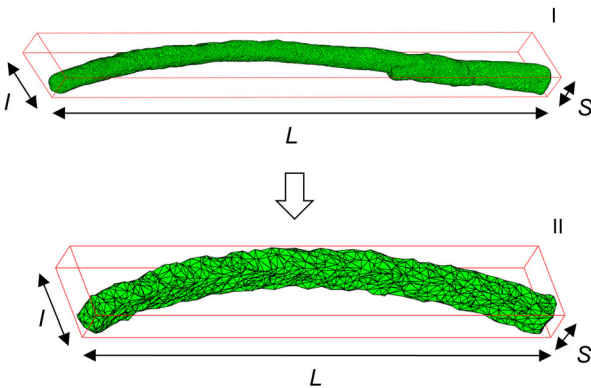
Figure 18. **Correctly classified firebrand B3-1: I. digital model with MBB; II. corresponding closest synthetic neighbor with MBB (models not to scale).**

Table 7
Descriptor Comparison Between the Misclassified Firebrands Shown in Fig. 11 (B2-1, B3-15) and a Selected, Correctly Classified Firebrand in the Rod-Bent Category (B3-1, See Fig. 18)

Case	Particle	Number #	E_l	F	E_q	S_{ph}	C_x	T
(a) See Fig. 11	Real	B2-1	0.11	0.62	0.07	0.37	0.23	0.48
	Synthetic	1573	0.16	0.61	0.10	0.40	0.29	0.38
(b) See Fig. 11	Real	B3-15	0.10	0.72	0.07	0.44	0.36	0.62
	Synthetic	1524	0.13	0.69	0.09	0.45	0.42	0.55
(c) See Fig. 18	Real	B3-1	0.09	0.46	0.04	0.40	0.35	0.80
	Synthetic	5812	0.16	0.41	0.07	0.45	0.38	0.78

"Real" and "Synthetic" refer to the firebrand digital model and its closest synthetic neighbor in the PCA space, respectively

SUPPLEMENTARY INFORMATION

The online version of this article (https://doi.org/10.1007/s10694-023-01530-4) contains supplementary material, which is available to authorized users.

References

1. Blanchi R, Leonard J (2005) Investigation of bushfire attack mechanism resulting in house loss in the ACT Bushfire 2003. https://www.bushfirecrc.com/sites/default/files/downloads/act_bushfire_crc_report.pdf
2. Maranghides A, Mell W (2009) A case study of a community affected by the Witch and Guejito fires. NIST Technical Note 1635. National Institute of Standards and Technology, Gaithersburg. https://doi.org/10.6028/NIST.TN.1635
3. Cohen JD, Stratton RD (2008) Home destruction examination—Grass Valley Fire, Lake Arrowhead, CA. Technical Paper R5-TP-026b. U.S. Department of Agriculture, Forest Service, Pacific Southwest Region (Region 5), Vallejo. https://www.fs.usda.gov/research/treesearch/31544
4. Graham R, Finney M, McHugh C, Cohen J, Calkin D, Stratton R, Bradshaw L, Nikolov N (2012) Fourmile canyon fire findings. General Technical Report RMRS-GTR-289. U.S. Department of Agriculture, Forest Service, Rocky Mountain Research Station, Fort Collins. https://doi.org/10.2737/RMRS-GTR-289
5. Ribeiro LM, Rodrigues A, Lucas D, Viegas DX (2020) The impact on structures of the Pedrógão Grande Fire Complex in June 2017 (Portugal). Fire 3(4):57. 10.3390/fire3040057
6. Barr BW, Ezekoye OA (2013) Thermo-mechanical modeling of firebrand breakage on a fractal tree. Proc Combust Inst 34(2):2649–2656. 10.1016/j.proci.2012.07.066
7. Woycheese JP, Pagni PJ, Liepmann D (1999) Brand propagation from large-scale fires. J Fire Prot Eng 10(2):32–44. 10.1177/104239159901000203
8. Sardoy N, Consalvi J-L, Porterie B, Fernandez-Pello AC (2007) Modeling transport and combustion of firebrands from burning trees. Combust Flame 150(3):151–169. 10.1016/j.combustflame.2007.04.008
9. Oliveira LA, Lopes AG, Baliga BR, Almeida M, Viegas DX (2014) Numerical prediction of size, mass, temperature and trajectory of cylindrical wind-driven firebrands. Int J Wildland Fire 23(5):698–708. 10.1071/WF13080
10. Tohidi A, Kaye NB (2017) Aerodynamic characterization of rod-like debris with application to firebrand transport. J Wind Eng Ind 168:297–311. 10.1016/j.jweia.2017.06.019
11. Mankame A, Shotorban B (2021) Deposition characteristics of firebrands on and around rectangular cubic structures. Front Mech Eng 7. https://doi.org/10.3389/fmech.2021.640979
12. Bearinger ED, Hodges JL, Yang F, Rippe CM, Lattimer BY (2021) Localized heat transfer from firebrands to surfaces. Fire Saf J 120:103037. 10.1016/j.firesaf.2020.103037
13. Abul-Huda YM, Bouvet N (2021) Thermal dynamics of deposited firebrands using phosphor thermometry. Proc Combust Inst 38(3):4757–4765. 10.1016/j.proci.2020.07.098
14. Ganteaume A, Lampin-Maillet C, Guijarro M, Hernando C, Jappiot M, Fonturbel T, Pérez-Gorostiaga P, Vega JA (2009) Spot fires: fuel bed flammability and capability of firebrands to ignite fuel beds. Int J Wildland Fire 18(8):951–969. 10.1071/WF07111
15. Panici D, de Almeida GAM (2018) Formation, growth, and failure of debris jams at bridge piers. Water Resour Res 54(9):6226–6241. 10.1029/2017WR022177

16. Luo J-Y, Xu Z-M, Ren Z, Wang K, Yang K, Tang Y-J, Gao H-Y, Tian L (2019) Rock avalanche-debris geometry and implications for rock-avalanche genesis. Geomorphology 334:60–75. 10.1016/j.geomorph.2019.02.029

17. Wang L, Jing H, Yu J, Liu X (2022) Impact of particle shape, size, and size distribution on gravity flow behaviour of broken ore in sublevel caving. Minerals 12(10):1183. 10.3390/min12101183

18. Hudson TR, Bray RB, Blunck DL, Page W, Butler B (2020) Effects of fuel morphology on ember generation characteristics at the tree scale. Int J Wildland Fire 29(11):1042–1051. 10.1071/WF19182

19. Thomas JC, Mueller EV, Santamaria S, Gallagher M, El Houssami M, Filkov A, Clark K, Skowronski N, Hadden RM, Mell W, Simeoni A (2017) Investigation of firebrand generation from an experimental fire: development of a reliable data collection methodology. Fire Saf J 91:864–871. 10.1016/j.firesaf.2017.04.002

20. Filkov A, Prohanov S, Mueller E, Kasymov D, Martynov P, Houssami ME, Thomas J, Skowronski N, Butler B, Gallagher M, Clark K, Mell W, Kremens R, Hadden RM, Simeoni A (2017) Investigation of firebrand production during prescribed fires conducted in a pine forest. Proc Combust Inst 36(2):3263–3270. 10.1016/j.proci.2016.06.125

21. Suzuki S, Manzello SL (2021) Towards understanding the effect of cedar roof covering application on firebrand production in large outdoor fires. J Clean Prod 278:123243. 10.1016/j.jclepro.2020.123243

22. Suzuki S, Manzello SL (2020) Garnering understanding into complex firebrand generation processes from large outdoor fires using simplistic laboratory-scale experimental methodologies. Fuel 267:117154. 10.1016/j.fuel.2020.117154

23. Hedayati F, Bahrani B, Zhou A, Quarles SL, Gorham DJ (2019) A framework to facilitate firebrand characterization. Front Mech Eng . 10.3389/fmech.2019.00043

24. Manzello SL, Suzuki S, Naruse T (2019) Quantifying wind-driven firebrand production from roofing assembly combustion. Fire Mater 43(1):3–7. 10.1002/fam.2661

25. Suzuki S, Manzello SL (2018) Characteristics of firebrands collected from actual urban fires. Fire Technol 54(6):1533–1546. 10.1007/s10694-018-0751-x

26. Suzuki S, Manzello SL (2016) Firebrand production from building components fitted with siding treatments. Fire Saf J 80:64–70. 10.1016/j.firesaf.2016.01.004

27. Suzuki S, Brown A, Manzello SL, Suzuki J, Hayashi Y (2014) Firebrands generated from a full-scale structure burning under well-controlled laboratory conditions. Fire Saf J 63:43–51. 10.1016/j.firesaf.2013.11.008

28. Suzuki S, Manzello SL, Hayashi Y (2013) The size and mass distribution of firebrands collected from ignited building components exposed to wind. Proc Combust Inst 34 (2):2479–2485. 10.1016/j.proci.2012.06.061

29. Suzuki S, Manzello SL, Lage M, Laing G (2012) Firebrand generation data obtained from a full-scale structure burn. Int J Wildland Fire 21(8):961–968. 10.1071/WF11133

30. Yoshioka H, Hayashi Y, Masuda H, Noguchi T (2004) Real-scale fire wind tunnel experiment on generation of firebrands from a house on fire. Fire Sci Technol 23 (2):142–150. 10.3210/fst.23.142

31. El Houssami M, Mueller E, Filkov A, Thomas JC, Skowronski N, Gallagher MR, Clark K, Kremens R, Simeoni A (2016) Experimental procedures characterising firebrand generation in wildland fires. Fire Technol 52(3):731–751. 10.1007/s10694-015-0492-z

32. Manzello SL, Maranghides A, Shields JR, Mell WE, Hayashi Y, Nii D (2009) Mass and size distribution of firebrands generated from burning Korean pine (*Pinus koraiensis*) trees. Fire Mater 33(1):21–31. 10.1002/fam.977

33. Manzello SL, Maranghides A, Mell WE (2007) Firebrand generation from burning vegetation. Int J Wildland Fire 16(4):458–462. 10.1071/WF06079

34. Vodvarka FJ (1969) Firebrand field studies. Final Technical Report J6148. IIT Research Institute, Chicago. https://apps.dtic.mil/sti/citations/AD0704725

35. Vodvarka FJ (1970) Urban burns—full scale field studies. Final Technical Report—Project J6171. IIT Research Institute, Chicago. https://apps.dtic.mil/sti/citations/AD0707454

36. Rissel S, Ridenour K (2013) Ember production during the Bastrop complex fire. Fire Manag Today 7–13. https://www.frames.gov/documents/usfs/fmt/fmt_72-4.pdf

37. Manzello SL, Foote EID (2014) Characterizing firebrand exposure from Wildland-Urban Interface (WUI) fires: results from the 2007 Angora fire. Fire Technol 50(1):105–124. 10.1007/s10694-012-0295-4

38. Zen S, Thomas JC, Mueller EV, Dhurandher B, Gallagher M, Skowronski N, Hadden RM (2021) Development of a field deployable firebrand flux and condition measurement system. Fire Technol 57(3):1401–1424. 10.1007/s10694-020-01074-x

39. Almeida M, Porto L, Viegas D (2021) Characterization of firebrands released from different burning tree species. Front Mech Eng 7. https://doi.org/10.3389/fmech.2021.651135

40. Filkov A, Prohanov S (2018) Particle tracking and detection software for firebrands characterization in wildland fires. Fire Technol 55(3):817–836. 10.1007/s10694-018-0805-0

41. Almeida M, Viegas DX, Raposo J (2014) Analysis of firebrand release on the spot fire mechanism. In: Viegas DX (ed) Advances in forest fire research 2014 Imprensa da Universidade de Coimbra, Coimbra, pp 61–72. 10.14195/978-989-26-0884-6_6

42. Tohidi A, Gollner MJ, Alfano C, Quarles Q (2017) Computer vision techniques for firebrand detection and characterization. In: 16th International conference on automatic fire detection and the suppression, detection and signaling research and applications (SUPDET 2017), Hyattsville, MD. https://www.nfpa.org/-/media/Files/News-and-Research/Resources/Research-Foundation/Symposia/2017-SUPDET/SUPDET17-Tohidi-et-al.ashx

43. Prohanov S, Filkov A, Kasymov D, Agafontsev M, Reyno V (2020) Determination of firebrand characteristics using thermal videos. Fire 3(4):68. 10.3390/fire3040068

44. Tohidi A, Kaye N, Bridges W (2015) Statistical description of firebrand size and shape distribution from coniferous trees for use in Metropolis Monte Carlo simulations of firebrand flight distance. Fire Saf J 77:21–35. 10.1016/j.firesaf.2015.07.008

45. Zingg T (1935) Beitrag zur Schotteranalyse. Schweizerische mineral petrogr Mitteilungen 15:39–140

46. Krumbein WC (1941) Measurement and geological significance of shape and roundness of sedimentary particles. J Sediment Res 11(2):64–72. 10.1306/D42690F3-2B26-11D7-8648000102C1865D

47. Sneed ED, Folk RL (1958) Pebbles in the Lower Colorado River, Texas—a study in particle morphogenesis. J Geol 66(2):114–150. 10.1086/626490

48. Pons MN, Vivier H, Belaroui K, Bernard-Michel B, Cordier F, Oulhana D, Dodds JA (1999) Particle morphology: from visualisation to measurement. Powder Technol 103(1):44–57. 10.1016/S0032-5910(99)00023-6

49. Blott SJ, Pye K (2008) Particle shape: a review and new methods of characterization and classification. Sedimentology 55(1):31–63. 10.1111/j.1365-3091.2007.00892.x

50. Anochie-Boateng J, Komba JJ, Tutumluer E (2012) Aggregate surface areas quantified through laser measurements for South African asphalt mixtures. J Transp Eng 138(8):1006–1015. 10.1061/(ASCE)TE.1943-5436.0000416

51. Sinecen M, Topal A, Makinaci M, Baradan B (2013) Neural network classification of aggregates by means of line laser based 3D acquisition. Expert Syst 30(4):333–340. 10.1111/j.1468-0394.2012.00638.x

52. Bagheri GH, Bonadonna C, Manzella I, Vonlanthen P (2015) On the characterization of size and shape of irregular particles. Powder Technol 270:141–153. 10.1016/j.powtec.2014.10.015

53. Miao Y, Yu W, Wu J, Wang S, Wang L (2019) Feasibility of one side 3-D scanning for characterizing aggregate shape. Int J Pavement Res 12(2):197–205. 10.1007/s42947-019-0025-0

54. Bhattacharya S, Subedi S, Lee SJ, Pradhananga N (2020) Estimation of 3D sphericity by volume measurement—application to coarse aggregates. Transp Geotech 23:100344. 10.1016/j.trgeo.2020.100344

55. Liu H, Sun Z, Li W, Huyan J, Guo M, Hao X (2020) Evaluating angularity of coarse aggregates using the virtual cutting method based on 3D point cloud images. IEEE Access 8:143241–143255. 10.1109/ACCESS.2020.3013901

56. Xie W-Q, Zhang X-P, Yang X-M, Liu Q-S, Tang S-H, Tu X-B (2020) 3D size and shape characterization of natural sand particles using 2D image analysis. Eng Geol 279:105915. 10.1016/j.enggeo.2020.105915

57. Loz PHF, Angulo SC, Rebmann MS, Tutumluer E (2021) Use of a 3D structured-light scanner to determine volume, surface area, and shape of aggregates. J Mater Civ Eng 33(9):04021240. 10.1061/(ASCE)MT.1943-5533.0003824

58. Parra-Denis E, Barat C, Jeulin D, Ducottet C (2008) 3D complex shape characterization by statistical analysis: application to aluminium alloys. Mater Charact 59(3):338–343. 10.1016/j.matchar.2007.01.012

59. Vecchio I, Schladitz K, Godehardt M, Heneka MJ (2012) 3D geometric characterization of particles applied to technical cleanliness. Image Anal Stereol 31(3):12. 10.5566/ias.v31.p163-174

60. Fonseca J, O'Sullivan C, Coop MR, Lee PD (2012) Non-invasive characterization of particle morphology of natural sands. Soils Found 52(4):712–722. 10.1016/j.sandf.2012.07.011

61. Yang X, Chen S, You Z (2017) 3D voxel-based approach to quantify aggregate angularity and surface texture. J Mater Civ Eng 29(7):04017031. 10.1061/(ASCE)MT.1943-5533.0001872

62. Zheng W, Hu X, Tannant DD, Zhang K, Xu C (2019) Characterization of two- and three-dimensional morphological properties of fragmented sand grains. Eng Geol 263:105358. 10.1016/j.enggeo.2019.105358

63. Garboczi EJ, Hrabe N (2020) Particle shape and size analysis for metal powders used for additive manufacturing: technique description and application to two gas-atomized and plasma-atomized Ti64 powders. Addit Manuf 31:100965. 10.1016/j.addma.2019.100965

64. Su D, Yan WM (2020) Prediction of 3D size and shape descriptors of irregular granular particles from projected 2D images. Acta Geotech 15(6):1533–1555. 10.1007/s11440-019-00845-3

65. Saxby J, Rust A, Beckett F, Cashman K, Rodger H (2020) Estimating the 3D shape of volcanic ash to better understand sedimentation processes and improve atmospheric dispersion modelling. Earth Planet Sci Lett 534:116075. 10.1016/j.epsl.2020.116075

66. Parra-Denis E (2007) 3D morphological analysis of complex shape particles: application to intermetallic particles in aluminium alloy. PhD Thesis, Université Jean Monnet, Saint-Etienne. https://tel.archives-ouvertes.fr/tel-00164990

67. Bouvet N, Link ED, Fink SA (2021) A new approach to characterize firebrand showers using advanced 3D imaging techniques. Exp Fluids 62(9):181. 10.1007/s00348-021-03277-6

68. Kapcak E (2015) Assessing firebrand collection methodologies. Final Report. FPInnovations—Wildfire Operations Research. https://library.fpinnovations.ca/en/permalink/fpipub9458

69. Gould J, McCaw W, Cheney N, Ellis P, Knight I, Sullivan A (2008) Chapter 10. In: Spotting behaviour and firebrand distribution, Project Vesta: fire in dry eucalypt forest—Fuel structure, fuel dynamics and fire behaviour. https://www.publish.csiro.au/book/5993/

70. Waterman TE (1969) Experimental study of firebrand generation. Final Technical Report—Project J6130. IIT Research Institute, Chicago. https://apps.dtic.mil/sti/citations/AD0695640

71. Zhou A, Quarles SL, Weise DR (2019) Fire ember production from wildland and structural fuels. Final Report. University of North Carolina-Charlotte, Insurance Institute for Business and Home Safety and Forest Service PSW-Forest Fire Lab-Riverside. https://www.firescience.gov/projects/15-1-04-4/project/15-1-04-4_final_report.pdf

72. Koo E, Pagni PJ, Weise DR, Woycheese JP (2010) Firebrands and spotting ignition in large-scale fires. Int J Wildland Fire 19(7):818–843. 10.1071/WF07119

73. Leventon IT, Tlemsani M, Hajilou M, Ju X, Gollner MJ (2021) Generation of firebrands from the burning of full-scale vegetation in the absence of ambient wind. Unpublished work

74. Aitkenhead A (2022) Mesh voxelisation, MATLAB Central File Exchange

75. Korsawe J (2022) Minimal Bounding Box, MATLAB Central File Exchange

76. Lehmann G, Legland D (2012) Efficient N-dimensional surface estimation using Crofton formula and run-length encoding. Insight J . 10.54294/wdu86d

77. Legland D (2022) Geodesic distances and geodesic diameters within 2D/3D images, MATLAB Central File Exchange

78. Lever J, Krzywinski M, Altman N (2017) Principal component analysis. Nat Methods 14(7):641–642. 10.1038/nmeth.4346

79. Ringnér M (2008) What is principal component analysis?. Nat Biotechnol 26(3):303–304. 10.1038/nbt0308-303

80. Jolliffe IT (2002) Principal component analysis, Springer series in statistics, Springer, New York. https://doi.org/10.1007/b98835

81. Jolliffe IT, Cadima J (2016) Principal component analysis: a review and recent developments. Philos Trans R Soc A 374(2065):20150202. 10.1098/rsta.2015.0202

82. Neal FB, Russ JC (2012) Measuring shape. CRC Press, Boca Raton. 10.1201/b12092

83. MATLAB (2022) The MathWorks Inc., Natick